# Chapter 11
# Microwave Tunable Properties of Microwire Composites

With a knowledge of the static properties of magnetic wires and their composites, we now usher this chapter into the dynamic properties of microwave composites at the gigahertz frequency range of application interest, i.e. microwave tunable properties. The main tunable events displayed here are all driven by external stimuli including dc magnetic field, tensile stress, and temperature. Although the mechanism varies for different types (or order of magnitude for magnetic field) of stimuli, the underlying physics is the same; that is, the microwires are excited by the incident EM wave and the variation of external field induces the change of skin effect or even ferromagnetic resonance in wires, resulting in the external field dependence of the frequency dispersion of EM parameters for the whole composite. But if we examine each composite with its varying structure, such as the local properties of wires (e.g. geometry and composition) and the topological arrangement of wires, some peculiar phenomena are observed. In the following, we treat categorically each type of tunable composite and give particular attention to the cases where unique field effects are exhibited.

## 11.1 Basic Theory of Field and Stress Tunable Properties

The microwave tunable properties of a microwire composite, by nature, are the response of effective permittivity to the electromagnetic wave through the surface impedance. Therefore, to explain this phenomenon, one needs to understand the basics of wave interactions with the materials and the effective medium approaches to characterise heterogeneous composites.

### *11.1.1 Effective Permittivity*

The effective permittivity should be treated differently in two types of composites that will be discussed in this chapter: those with short wires and those with long



H.-X. Peng et al., *Ferromagnetic Microwire Composites*,
Engineering Materials and Processes, DOI 10.1007/978-3-319-29276-2_11

wires. In composites containing short wires, the Lorentz model proves to be effective, whereas the Drude model is applicable to composites containing long wires. The Lorentz model is first considered to be applicable to all insulator materials. Along the inclusion length, the current with a linear density $j(x)e^{-i\omega t}$ is induced by the local electrical field $e_{\mathrm{loc}}\exp(-i\omega t)$. Using the continuity equation and integration by parts with boundary conditions, the electric dipole moment $D$ can be calculated as:

$$D = \frac{i}{\omega}\int_{1/2}^{1/2} j(x)\mathrm{d}x \Rightarrow \alpha = \frac{D}{Ve_{\mathrm{loc}}}, \tag{11.1}$$

where $l$ is the length of the wire and $V$ is the inclusion volume. Within the frame of this approach, the dielectric polarisability $\alpha$ of the inclusion can also be calculated [1]:

$$\alpha(\omega) = \sum_n \frac{A_n}{(\omega_{\mathrm{res},n}^2 - \omega^2) - i\Gamma_n\omega}, \tag{11.2}$$

where $\omega_{\mathrm{res},n}$ is the angular resonance frequency, $A_n$ are amplitude constants, and $\Gamma_n$ are the damping parameters. $A_1$ contributes most to the polarisability corresponding to the lowest frequency. $\Gamma_n$ is considerably influenced by the resistive magnetic losses [2], and it presents a strong dependence on the external magnetic field or stress in the vicinity of an antenna resonance in certain conditions. An experimental proof of this equation has been provided in Refs. [3] and [4].

The bulk polarisation of the composites can be expressed as:

$$P = \langle e_{\mathrm{loc}}\rangle p_v\alpha = e_0\chi_{\mathrm{eff}}, \tag{11.3}$$

where $e_{\mathrm{loc}}$ is the averaged local field, $p_v$ is the volume concentration of the inclusions, $e_0$ is the external electric field, and $\chi_{\mathrm{eff}}$ is the effective bulk susceptibility. When $p_v \ll p_c$, it follows that $e_{\mathrm{loc}}c \approx e_0$ [5]. Thus, the effective permittivity can be obtained by:

$$\varepsilon_{\mathrm{eff}} \approx \varepsilon + 4\pi p_v\langle\alpha\rangle \tag{11.4}$$

where $\varepsilon$ is the permittivity of the matrix and $\langle\alpha\rangle$ is the averaged polarisability of an individual inclusion. Further calculations involve the GMI effect and surface impedance of wires, which are presented in the following section.

For continuous-wire composites, charge distribution along the wire axis is absent, and hence, no current or dipole response exists. It can then be treated as a medium with diluted plasma according to Pendry et al. [6]. Thus, the dispersion of

effective permittivity for this kind of composite is characterised by the plasma frequency expressed as:

$$\omega^2 = \frac{2\pi c^2}{b^2 \ln(b/a)}, \tag{11.5}$$

where $b$ is the wire period. In this context, the deduction of effective permittivity can be approached by solving the Maxwell equations in a homogenisation procedure as the wire parameters have no influence on the permittivity. For a non-magnetic wire composite, the effective permittivity can be given by [7]:

$$\begin{aligned} \varepsilon_{\text{eff}} &= \varepsilon - p_v \frac{2\varepsilon_c F_1(k_c a)}{(ak_c)^2 F_1(k_c a)\ln(L/a) - 1}, \\ F_1 &= J_1(x)/xJ_0(x), \left| p_v = \pi a^2/L^2, \right. \\ \varepsilon_c &= 4\pi i\sigma/\omega\, k_c = 4\pi i\omega\sigma/c^2, \end{aligned} \tag{11.6}$$

where $p_v$ is the wire volume concentration, $\varepsilon_c$ is the dielectric permittivity of the conductor, $\sigma$ is the wire conductivity, $k_c$ is the wave number, and $J_{0,1}$ are Bessel functions. At microwave frequency, there is a very strong skin effect, i.e. $ak_c \sim a/\delta \gg 1$. Thus, Eq. 11.6 can be reduced to Eq. 11.5, justifying the application of the model for continuous-wire composites. As with short-wire composites, impedance should be calculated first.

### 11.1.2 Impedance Tensor

The surface impedance is a parameter to characterise the voltage response in the wire system, as described in the GMI phenomenon. To calculate the impedance tensor in the wire, the electromagnetic conditions about the wire should be fully understood. Figure 11.1 shows the current $e_x$ along the wire axis direction inducing the circular field $h_\phi$, of which the tangential component $h_{x,0}$ plus the external field induce the electric field $e_\phi$. In this case, the response to the electromagnetic field from the wire via the impedance tensor with the boundary conditions can be written as follows [8]:

$$\overline{E_t} = \zeta(\overline{H_t} \times n), \tag{11.7}$$

where **n** is the unit normal vector directed inside the wire, $\overline{E_t}$ and $\overline{H_t}$ are the tangential vectors of the total electric and magnetic fields at the wire surface, including both scattered and external fields. Adopting the typical simplified

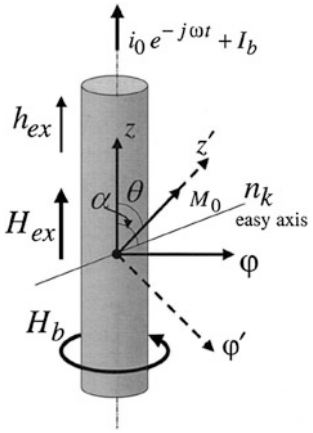


**Fig. 11.1** Schematic diagram of the magnetic configuration in a wire. Reprinted with permission from [9], copyright 2005 Nova Science

approach for antenna problems, Eq. 11.7 can be written in polar coordinates $(x, \phi)$ [9]:

$$\begin{aligned} \overline{E_x} &= \varsigma_{xx}\overline{H_\phi} - \varsigma x\phi\overline{H_x}, \\ \overline{E_\phi} &= \varsigma_{\phi x}\overline{H_\phi} - \varsigma_{\phi\phi}\overline{H_x}. \end{aligned} \tag{11.8}$$

### 11.1.3 Stress and Field Dependence of Impedance and Permittivity

For short-wire composites, it follows from Eq. 11.4 that the averaged polarisability needs to be worked out. When the interactions between the wires are reasonably neglected, it can be derived as [10]:

$$\begin{aligned} \langle\alpha\rangle &= \frac{1}{2\pi\ln(1/a)(ka)^2}\left(\frac{2}{kl}\tan(kl/2) - 1\right), \\ k &= \omega\frac{\sqrt{\varepsilon}}{c}\left(1 + \frac{ic\varsigma_{xx}}{\omega\alpha\ln(1/a)}\right)^{1/2}. \end{aligned} \tag{11.9}$$

It should be noted that the equations right above are established in the frame of the composites in question with a moderate skin effect, under which the radiation loss is overshadowed by the magnetic and resistive losses.

It can be seen from Eqs. 11.4 and 11.9 that the permittivity depends on the surface impedance in this case. Due to the GMI effect as previously analysed, the dependence of permittivity through impedance on the external field is well established according to Eq. 11.12.

In the case of long-wire composites, Eq. 11.6 was extended to approach the case of magnetic wires. By substituting the impedance formula, Eq. 11.6 is transformed to [11]:

$$\varepsilon_{\text{eff}} = \varepsilon - p_v \frac{w_p^2}{w^2\left(1 + i\frac{c\varsigma_{xx}}{wa\ln(b/a)}\right)}. \tag{11.10}$$

Thus, the effective permittivity for continuous-wire composites is dependent on the wire surface impedance via the plasma frequency.

Due to the amorphous structure of the microwires, their anisotropy is dominated by the magnetoanisotropy coupled with the internal and/or external stress and magnetostriction, but the shape anisotropy makes no contribution. The influence of internal stress and applied stress on GMI has been reported theoretically in [12] and [13]. Regarding the glass-coated microwires, the following equations are held:

$$K = K_0 - 1.5\lambda(\sigma_{zz} - \sigma_{\phi\phi} + \sigma_{\text{applied}}), \tag{11.11a}$$

and

$$H_k = 2K/\mu_0 M_s, \tag{11.11b}$$

where $K$ and $H_k$ are the anisotropy constant and field, respectively; $\sigma_{zz}$, $\sigma_{\phi\phi}$, and $\sigma_{\text{applied}}$ are the axial, azimuthal stress, and applied stress, respectively; $M_s$ is the saturation magnetisation; and $\mu_0$ the permeability in vacuum. Also the effective permeability depends on the ratio of $H_k$ to $M_s$, which is determined by $K$, expressed as [14]:

$$\mu_{\text{eff}} = \frac{M_s \sin^2(\theta + \theta_e)}{H_k\left[h\sin^2(\theta + \theta_e) + \cos(2\theta)\right]}, \tag{11.12}$$

where the anisotropy field $H_k = 2\,K/M_s$ and $h = H_{ex}/H_k$. $\theta$ is between the anisotropy angle $\theta_e$ and $\pi/2$. Besides, the static magnetisation angle also changes with the anisotropy angle, as indicated in the equation for the magnetostatic energy $U_m$ based on the equivalent uniaxial anisotropy [15]:

$$U_m = -|K|\cos^2(\alpha - \theta) - M_0 H_{ex}\cos\theta, \tag{11.13a}$$

$$|\widetilde{K}| = \frac{K + (3/2)\lambda\sigma_a}{\cos(2\widetilde{\alpha})}, \tag{11.13b}$$

$$\widetilde{\alpha} = \frac{1}{2}\tan^{-1}\frac{3|\lambda\sigma_t|}{|K + (3/2)\lambda\sigma_a|}, \tag{11.13c}$$

where $\alpha$ is the anisotropy angle, which takes different values according to the relationship between the anisotropy constant $K$ and the product of magnetostriction constant $\lambda$ multiplying the axial stress $\sigma_a$ [10].

The tunable properties can be characterised by the free-space measurement. From what has been discussed above, the dependencies of effective permittivity through magnetoimpedance on the field and stress are well established. A note is in order here. Such metal–dielectric composites incorporating wire-shaped inclusions have been treated theoretically and experimentally for decades [16]. Most recently, researchers have found that it is possible to obtain a negative permittivity and/or permeability at certain frequencies for this kind of composite and recognised its importance [17]. This brings about the next important functionality of the wire composite, i.e. metamaterial properties, which will be discussed in the following section. Further to the understanding of the GMI/GSI behaviours of microwires and their composites, this section targets the microwave tunable properties of the microwire composites, i.e. tunable electromagnetic properties by magnetic field [2, 9, 11, 18–26], stress [9–11, 15, 27], and temperature [18, 19]. The tunable property is actually the so-called cross-variable response unique to multifunctional composites, i.e. a given field can control two or more variables, or a variable can be switched by two or more external fields. To achieve such tenability or adjustability is essential for microwave applications such as tunable microwave devices [9] and remote-interrogated sensors [28]. It will also be called for to realise reconfigurable local network environments, beam-steering antennas, and microwave remote sensing and control. Most of the proposed methods have been based on biased ferroelectric, ferrite, or magnetic composite substrates and reconfigurable resonant elements implementing active devices or a system of microactuators [29–31]. These technologies each have their advantages and limitations, such as high power consumption, low operational speed, limited frequency band, and high cost. Dilute composites with ferromagnetic microwires were proposed in this context by Panina et al. [9, 11]. Together with the following studies [21, 22, 24–27, 32], the possibility of tailoring the collective dielectric response of the wire media by changing the local magnetic properties with external stimuli without changing the structural parameters has been demonstrated.

In what follows, after a brief introduction of the measurement techniques, the tunable properties will be discussed in three categories: magnetic field tunable properties, stress tunable properties, and temperature tunable properties. In each section, both the wires and their composites will be discussed. Note that all the composites under discussion here are non-percolating due to either the periodical arrangement of the wires with fixed spacing or the existence of glass coating for random-wire composites. Thus, there is no concern that the formation of a conductive network will hinder their interactions with the microwave.

## 11.2 Measurement Techniques

### *11.2.1 Free-Space Measurement System*

Investigation of the microwave tunable properties of composites was carried out in free space using the standard calibration technique named through-reflection-line (TRL), as a well-received testing method for dielectric materials and any non-coaxial measurements of *S*-parameters [33–37]. The schematic graph of the measuring system employed for our experiments is shown in Fig. 11.2 [38]. To neutralise the influences of the noises on the scattering, the walls of the compact anechoic chamber are made of plywood and covered on the inside by a microwave absorber and a network analyser with which the time-domain option is employed [34, 39, 40]. Antennas are connected to the ports of a HP8720ES spectrum network analyser through RG402 cables with Subminiature version A (SMA) connectors (see Fig. 11.3) [18]. The detailed features of the antennas are as follows: (1) length: 887 mm; (2) aperture: 351 × 265 mm; (3) frequency range: 0.85–17.44 GHz; (4) standing-wave ratio (SWR) < 1.7; (5) effective area > 150 $mm^2$ in the range of 0.85–15 GHz.

The distance between antennas is controllable with the mobile front walls of the chamber where the antennas are fastened to meet the requirement of preliminary TRL calibration. The frame's function is to guarantee the uniform heating or magnetic field along the sample surface when the microwave response depends on

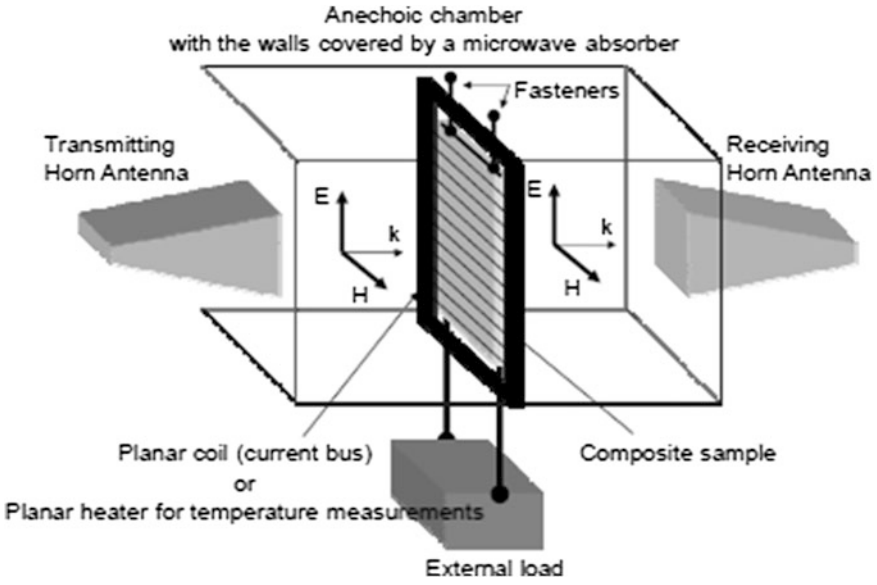


**Fig. 11.2** Free-space measuring system. Two types of external action were applied to the sample: tensile stress and dc magnetic field. Reprinted with permission from [41]

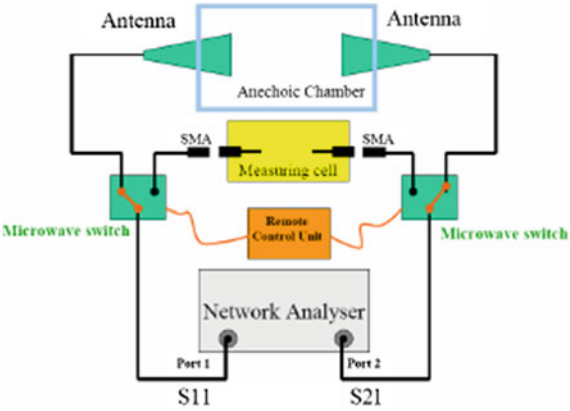


**Fig. 11.3** The scheme of measuring track showing the option of switching between chamber and cell. Reprinted with permission from [41]

the external stimuli including field, stress, and temperature. A current bus or a planar coil was used for the same reason and also makes the composites easily tunable by a weak magnetic field. It is highlighted that the parallel current wires must be oriented perpendicularly to the vector of the electrical field in the plane-polarised accidental electromagnetic wave in order to allow for nothing but the interaction between the composites and electromagnetic wave. Note that the design of the switch makes the most of the analyser, between the non-contact microwave test in the anechoic chamber and the contact test on magnetic wires in the measuring cell (Fig. 11.3) [18, 38].

If a very high magnetic field is required, the planar coil is preferred to the current bus because all turns in a coil are connected in series, thus passing the total current. The construction of the frame out of planar coil is shown in Fig. 11.4. The sample is placed between the two coil layers. The complex permittivity can be computed from the *S*-parameters collected from the measurement. *S*-parameters $S_{11}$ and $S_{21}$ can be expressed via reflection coefficient $\Gamma$ and transmission coefficient $T$ as [33]:

$$S_{11} = \frac{\Gamma(1 - T^2)}{1 - \Gamma^2 T^2}, \tag{11.14a}$$

and

$$S_{21} = \frac{T(1 - T^2)}{1 - \Gamma^2 T^2}. \tag{11.14b}$$

$\Gamma$ and $T$ can then be calculated by:

$$\Gamma = \frac{(Z_{sn} - 1)}{(Z_{sn} + 1)}, \tag{11.15a}$$

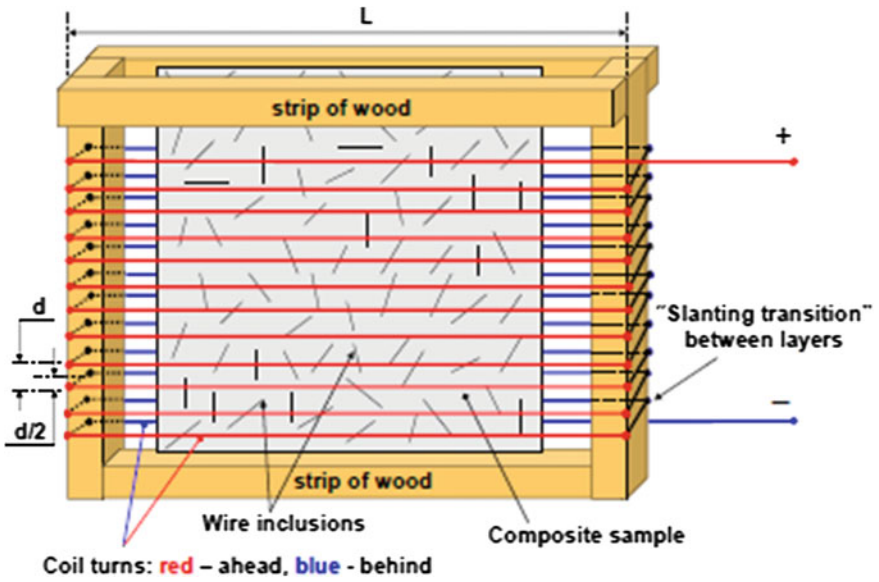


**Fig. 11.4** The construction of a planar coil for laboratory investigations. The composite sample is placed in between two coil layers. The coil becomes "invisible" for a plane-polarised wave with the electrical vector directed transversely to the coil turns, as shown in Fig. 11.2. To provide the uniform magnetic field inside the coil, the distance between the coil layers must be equal to the interturn distance $d$, and these layers must be shifted transversely across one another over steps of $d/2$. Reprinted with permission from [41]

and

$$Z_{sn} = (1/\sqrt{\varepsilon^*})T = e^{-\gamma d}, \gamma = (2\pi/\lambda_0)(\varepsilon^*)^{1/2}, \tag{11.15b}$$

where $\lambda_0$ is the wavelength in the free space and $d$ is the thickness of the sample. The complex permittivity is given by:

$$\varepsilon^* = \frac{\gamma}{\gamma_0}\left(\frac{1-\Gamma}{1+\Gamma}\right). \tag{11.16}$$

### *11.2.2 Microwave Frequency-Domain Spectroscopy*

A modified microwave frequency-domain spectrometer is shown in Fig. 11.5. Figure 11.5a shows the instrument specifically designed to study the effects of stresses or magnetic field on the samples. A strain as large as 100 % is obtainable if within the flexibility of the sample. The extension was measured with a hand gauge. The samples were mounted strictly along the direction of stress applied. A solenoid

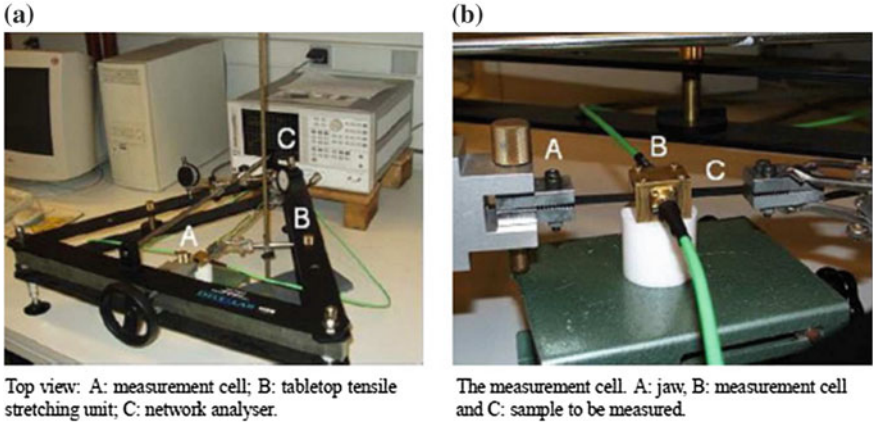


**Fig. 11.5** Photographs of instrumentation for microwave measurements. Reprinted with permission from [42], copyright 2005 IOP

can be easily set up to allow a measurement in the presence of magnetic field along the wave propagation direction.

Figure 11.5b illustrates the perspective view of the measurement cell. With *S*-parameters measured by the network analyser, the permittivity and permeability can be extracted by a utility program. Note that this instrument is capable of simultaneous measurement of electric permittivity and magnetic permeability in the presence of magnetic field and/or stress at a very wide spectra coverage up to gigahertz.

Full details of the design and specification of this spectroscopy can be found in Ref. [43]; herein only a brief summary will be provided. In outline, the microwave characterisation using this equipment consists of measuring the transmission and reflection coefficients of an asymmetric microstrip transmission line containing the tested sample in the presence of a magnetic bias or tensile stress.

The measurement of the scattering parameters (*S*-parameters) was achieved using an Agilent H8753ES network analyser with short-open-load-thru (SOLT) calibration. A utility program extracts the data and generates complex permittivity $\varepsilon$ and magnetic permeability spectra as individual files in .txt format. As outlined in [42], the quasi-transverse electric and magnetic mode, which is the only mode that propagates in the structure, makes analysis of the complex transmission and reflection coefficients created by the discontinuity between the line and the sample relatively uncomplicated. Using the Nicolson–Ross procedure for the transformation of the load impedance by a transmission line, $e$ is determined by the transmission $S_{21}$ and reflection $S_{11}$ parameters. An error analysis indicates modest uncertainties in $\varepsilon'$, $\mu'$ (<5 %) and $\mu''$, $\mu''$ (<1 %) for the data. One further feature of the measurement system is worth commenting on. To obtain accurate measurements of $\varepsilon$ and $\mu$, it is particularly important to account for the residual air-gap between the sample and the line walls; that is, the gap is determined by the roughness of the surfaces of the measured samples.

## 11.3 Low-Field Tunable Properties

### *11.3.1 Field Effect on the Impedance of Single Wire*

The static magnetic field is essential to generate the GMI effect. With our focus on the gigahertz frequency range, the numerous studies on the megahertz frequency range (see [44] and references therein) will be skipped. At high frequency, the GMI effect is believed to be caused by the natural ferromagnetic resonance in the outer layer of wires occurring at a relatively small ac field [45–48]. The resonance frequency is dependent on the anisotropy field, anisotropy angle, and external field (if it exists) [10, 15, 21, 49, 50]. At around resonance frequency, the field sensitivity can reach a maximum [51]. The typical field effect is shown in Fig. 11.6. Note that the real (imaginary) part of $Z$ corresponds to the imaginary (real) part of circumferential permeability [48]. Similar effects are also shown elsewhere [52–55].

### *11.3.2 Continuous-Wire Composites*

For continuous-wire composites, the dependence of effective permittivity on the external field is established via the field dependence of plasma frequency according to Eq. 11.10. As the plasma frequency is dependent on the interwire spacing and wire diameter following Eq. 11.5, these two geometrical parameters are critical in governing the effective response of the composite to the external field. Actually, this is quite reasonable since these two parameters constitute the basic mesostructure and are decisive in the dielectric heterogeneous composites [56–58]. Also, the tunable properties are largely determined by the local magnetic properties

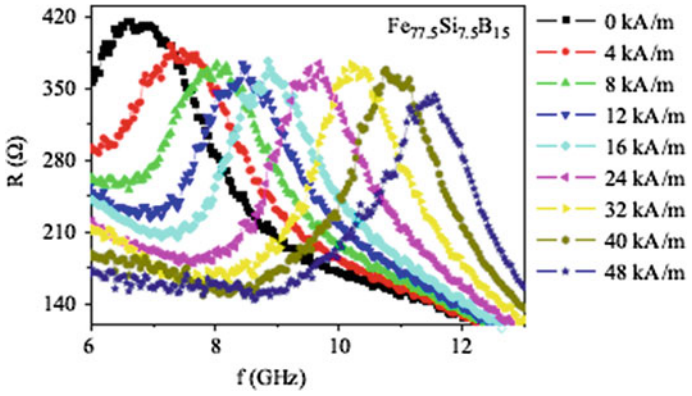


**Fig. 11.6** Real component of impedance for a FeSiB glass-coated microwire as a function of frequency for selected values of applied field. Reprinted with permission from [50], copyright 2009 Elsevier

of the wires. Therefore, the following discussion of tunable properties of continuous-wire composites is carried out from these three critical influencing factors, i.e. interwire spacing (also known as cell parameter, periodicity), wire diameter, and local magnetic property of wires.

#### 11.3.2.1 Influence of Wire Periodicity

Figure 11.7 displays the dependence of complex effective permittivity on the frequency, with magnetic field as a parameter for composites with wire $Co_{68.7}Fe_4Ni_1B_{13}Si_{11}Mo_{2.3}$ with different periodicity. The dependence of the effective permittivity is well displayed in both graphs below the corresponding plasma frequency.

It can also be seen that, with increasing wire periodicity from 7 to 15 mm, the frequency dispersion of effective permittivity on the magnetic field is remarkably depreciated as the tunability (defined as the ratio of variation of the electromagnetic parameter to that of the corresponding field [29]) is reduced from 0.16 m/A to $7.7 \times 10^{-3}$ m/A. This means that a small wire periodicity is preferable for a field tunable property. However, a decrease of wire periodicity will increase the plasma frequency and hence the skin effect. If the skin effect is too strong, the field effect will be rather weak. Therefore, the wire diameter may also need to be decreased to

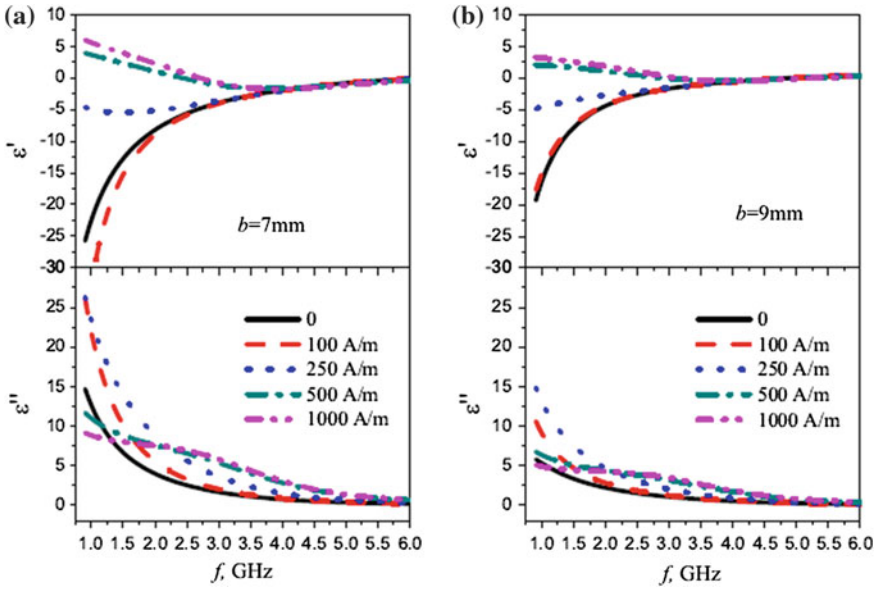


**Fig. 11.7** Frequency plots of the real and imaginary part of effective permittivity for composites containing long continuous wires with the external field as a parameter. **a** Wire spacing $b = 7$ mm; **b** $b = 9$ mm. Reprinted with permission from [59], copyright 2012 Elsevier

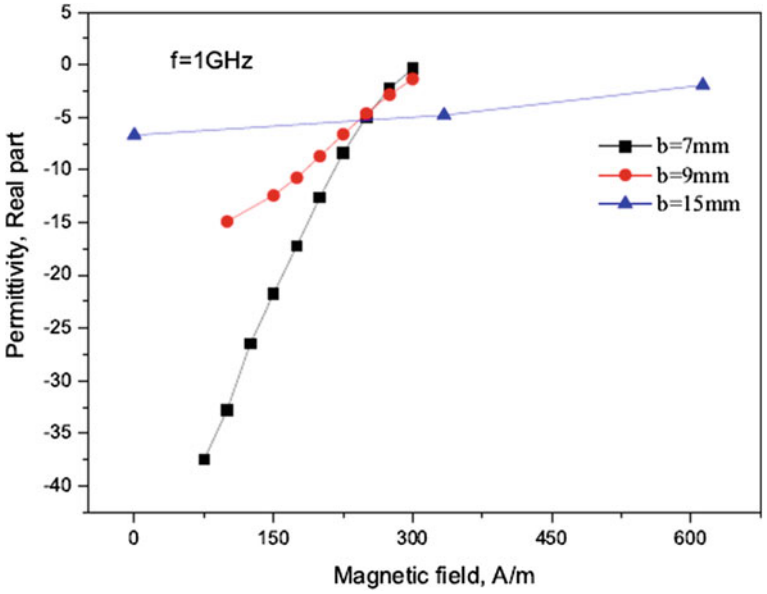


**Fig. 11.8** Effective permittivity, real part, as a function of external field for composites containing continuous wires with different wire periodicity $b$ = 7, 9, and 15 mm. Reproduced with permission from [59], copyright 2012 Elsevier

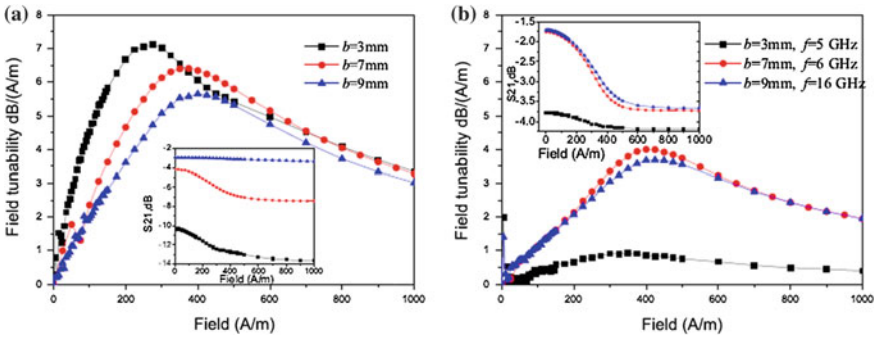


**Fig. 11.9** Field tunability of transmission parameter $S_{21}$ as a function of external field for composites containing continuous wires with different wire periodicity $b$ = 3, 7, and 9 mm at (**a**) 4 GHz and (**b**) plasma frequencies for each wire periodicity. The ordinate profiles are divided by the factor 0.001. *Inset graphs* are the corresponding field dependence of $S_{21}$. Reprinted with permission from [22], copyright 2010 AIP

compensate the decrease of skin depth. Thereby, there exists an optimum value of wire periodicity matching the diameter for the microwave tunable properties. This is consistent with the theoretical prediction that for $b$ = 0.5 mm, the best tunability will be achieved for a wire radius of 5–10 μm [60] (see Figs. 11.8 and 11.9).

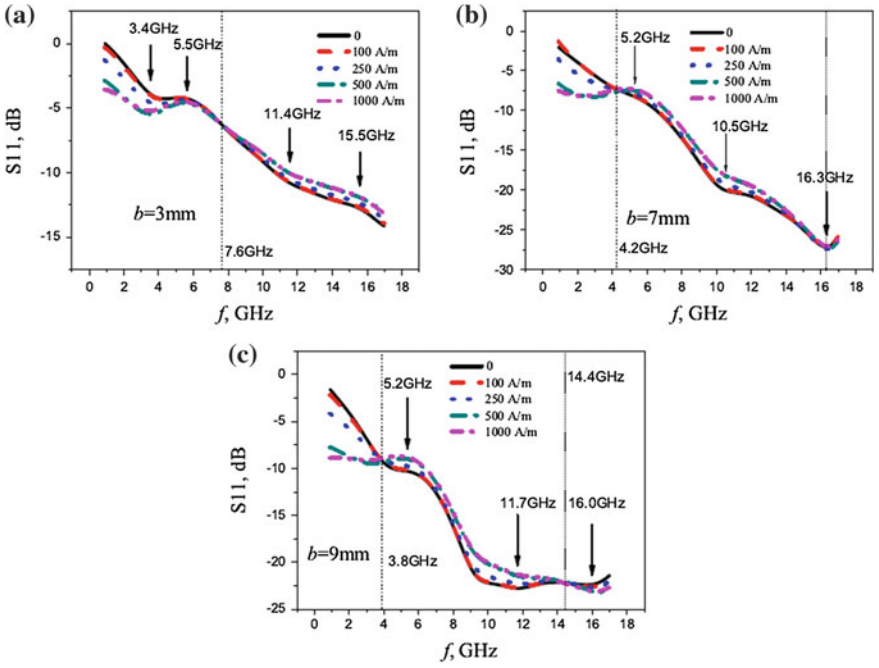


**Fig. 11.10** Experimental reflection spectra ($S_{11}$) for composite sample of 640 μm thick and 50 cm × 50 cm in-plane size with continuous amorphous wires spaced at 3 mm (**a**), 7 mm (**b**), and 9 mm (**c**). Reprinted with permission from [59], copyright 2012 Elsevier

Figure 11.10 shows the frequency dependence of the reflection parameter ($S_{11}$) taken at different magnetic fields for the composites with $b$ = 3, 7, and 9 mm. It can be seen that the shape of the curves varies remarkably as the wire periodicity increases from 3 to 9 mm. For the $b$ = 3-mm sample, the spectra can be divided into two frequency zones at 7.6 GHz. Below 7.6 GHz, the reflectivity decreases as the magnetic field is applied. This is due to the absorption effect. However, the opposite trend is observed for $f > 7.6$ GHz. For the $b$ = 7- and 9-mm samples, one more zone is found for $f > 16.3$ GHz and $f > 14.4$ GHz. The frequency at which the signal of $S_{11}$ changes with magnetic field is considered the characteristic frequency. It is worth noting here that as $b$ increases from 3 to 9 mm, the characteristic frequency decreases from 7.6 to 3.8 GHz (between zones 1 and 2). One can also see that the characteristic frequency (between zones 2 and 3) decreases from 16.3 GHz for the $b$ = 7-mm sample to 14.4 GHz for the $b$ = 9-mm sample. For the $b$ = 3-mm sample, the characteristic frequency cannot be determined due to the limited measurement frequency range, but it appears to be higher than those for the $b$ = 7- and 9-mm composites. This finding points to an important consequence that the characteristic frequency shifts to a lower value for composites with larger wire periodicity in the reflection spectra.

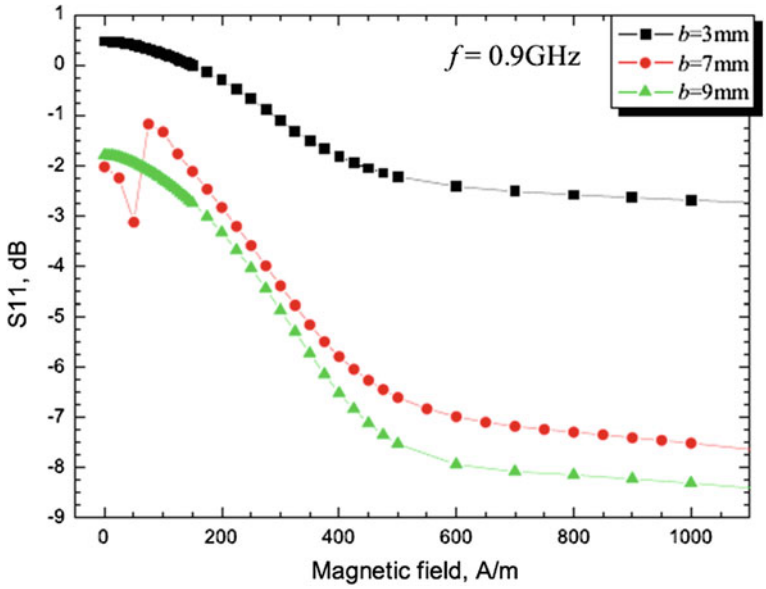


**Fig. 11.11** Reflection parameter as a function of external field for composites containing continuous wires with different wire periodicity $b$ = 3, 7, and 9 mm at the initial frequency of 0.9 GHz

Figure 11.11 shows the magnetic field dependence of the reflection parameter ($S_{11}$) taken at 900 MHz. The sensitivity of $S_{11}$ to the magnetic field is positively correlated to $b$. For the composites with $b$ = 9 mm, $S_{11}$ falls from −1.8 dB at Hex = 0 to −7.5 dB at Hex = 500 A/m.

#### 11.3.2.2 Influence of Wire Diameter

It is well known that the wire diameter has a strong impact on the GMI properties of microwires [61–64]. Figure 11.12 shows that composites containing wires with a larger diameter present a higher-field tunability than those with a smaller diameter, which can be explained by the wire geometry dependence of the GMI effect and associated skin effect. It has already been demonstrated that the GMI effect is positively correlated to the wire diameter [65]. Accordingly, the dielectric response of the composite containing wires of larger diameter is stronger than otherwise [2].

A comparison between the transmission spectra (cf. Fig. 11.13) reveals that the diameter of the wire has a profound impact on the intensity of $S_{21}$ but much less effect on the tunability. The variation of diameter of several microns has a negligible influence on the plasma frequency of 5 GHz, and the frequencies at which $S_{21}$ reaches the minimum are about 3 GHz for both of them. It follows that the plasma frequency probably decides the patterns of transmission spectra. The phase shift of

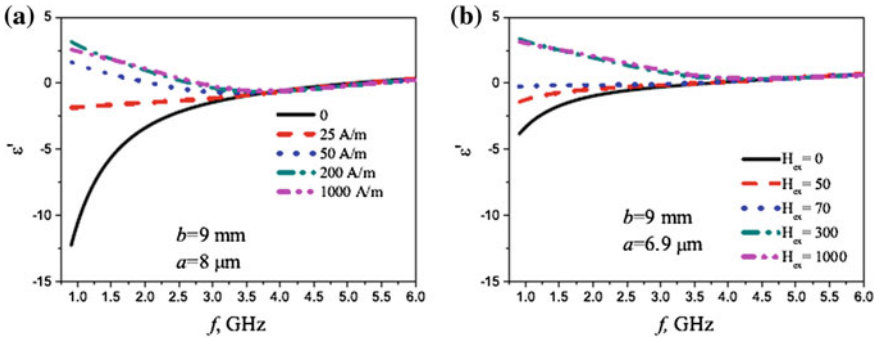


**Fig. 11.12** Frequency dependence of real part of effective permittivity with external field as a parameter for composites containing wires of different radius $a$. Reproduced with permission from [59], copyright 2012 Elsevier

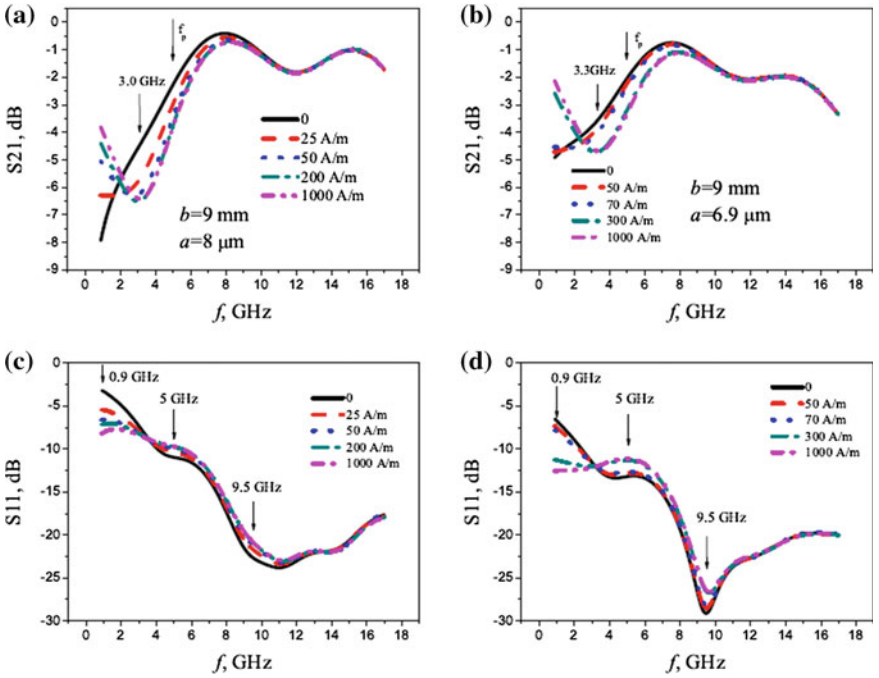


**Fig. 11.13** Frequency dependence of $S$-parameters with external field as a parameter for composites containing wires of different radius: (**a**, **c**) $a$ = 8 μm; (**b**, **d**) $a$ = 6.8 μm. Reproduced with permission from [59], copyright 2012 Elsevier

$S_{11}$ in the presence of an external field (*cf.* Fig. 11.14) suggests a promising sensing application of the composite. For the composite with 8-μm-thick wire, the phase going through $\pm\pi$ is completely suppressed when it is under a small field of 25 A/m.

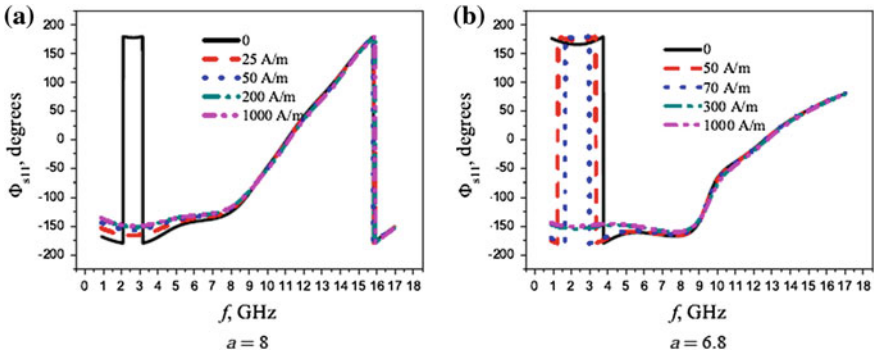


**Fig. 11.14** Frequency dependence of phase of $S_{11}$ with external field as a parameter for composites containing wires of different radius. Reproduced with permission from [59], copyright 2012 Elsevier

For the composite with 6.8-μm-thick wire, the concerned phase shifts to a lower value, from 3.7 in the absence of a field to 3.0 in the presence of a field of 70 A/m. These considerable changes suggest that the ferromagnetic microwires enable their composite with a self-monitoring capacity: any stress change that occurs to the wire through the composite can be detected via the microwave tunable spectra.

#### 11.3.2.3 Influence of Wire Composition

Following from the very strong dependence of the GMI property on the composition of microwires [44, 63, 64, 66], the change of local magnetic properties with the composition is expected to vary the field effect. Figure 11.15 shows a comparison between the composites containing wires of the same geometry but different composition. The two wire composites present rather good dispersion properties but differing field effects. The scattering spectra for the two composites with a periodicity of 7 mm are presented in Fig. 11.16. In the spectra of $S_{11}$, the two composites possess almost the same characteristic frequencies but differing field tunability. All these observed effects are attributed to the difference in soft magnetic properties. Specifically, $Co_{68.7}Fe_4Ni_1B_{13}Si_{11}Mo_{2.3}$, with a better soft magnetic property than the other composition, has a larger dynamic magnetic permeability $\mu$ at the concerned frequency range, giving rise to a larger relaxation parameter $\gamma$ according to $\gamma \propto \sqrt{\mu}\cos^2\theta$ [60] where $\theta$ is the static magnetisation angle. As it has been proved that field tunable effects are positively dependent on the relaxation parameter, the excellent magnetic softness would be preferable to realise strong field tunable effects. In considering that the soft magnetic features of microwires are sensitive to the composition [67, 68], one should try to achieve a precise control of composition in the fabrication process and appropriate tailoring in the post-fabrication treatments before proceeding to the manufacture of microwire composites for field tunable functionality.

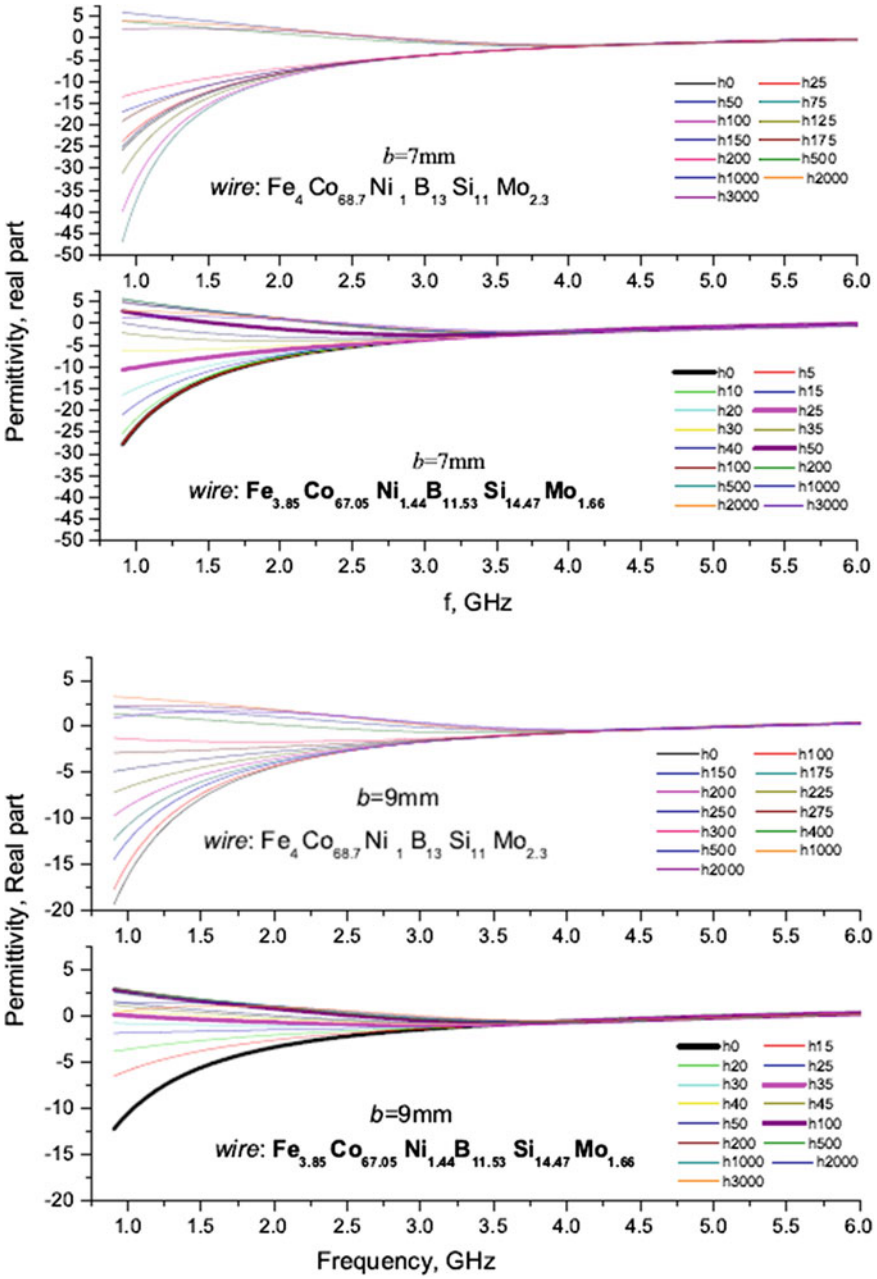


**Fig. 11.15** Frequency plots of the effective permittivity, real part, for composites containing long continuous wires ($Co_{68.7}Fe_4Ni_1B_{13}Si_{11}Mo_{2.3}$ and $Co_{67.05}Fe_{3.85}Ni_{1.44}B_{11.53}Si_{14.47}Mo_{1.66}$) with the external field $H_{ex}$ as a parameter. Wire radius $a$ = 10 μm; wire periodicity $b$ = 7 mm (*upper plot*) and $b$ = 9 mm (*lower plot*). Reprinted with permission from [69], copyright 2013 Elsevier

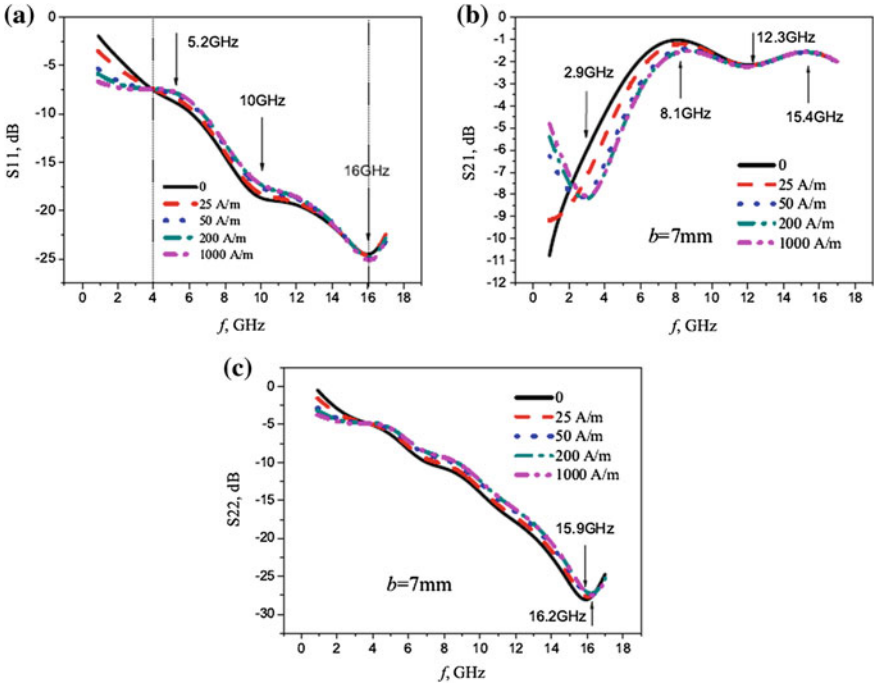


**Fig. 11.16** Frequency dependencies of magnitude of *S*-parameters for composite containing amorphous wires $Co_{67.05}Fe_{3.85}Ni_{1.44}B_{11.53}Si_{14.47}Mo_{1.66}$ spaced at 7 mm. (**a**) $S_{11}$, (**b**) $S_{21}$, and (**c**) $S_{22}$. Reprinted with permission from [69], copyright 2013 Elsevier

### *11.3.3 Short-Wire Composites*

In a short-wire composite, short wire pieces may be uniformly dispersed in a random manner [24–26] or in a periodical manner [21, 22, 27, 32, 70–72]. In this section, the magnetic bias (field) effects of short-wire composites are presented and discussed within the theoretical framework detailed in Sect. 11.1.

Figure 11.17 shows the dispersion of effective permittivity for a short-wire composite with the parameters ($l$, $a$, $n_c$) detailed in the graph. The value of $\varepsilon'$ is rather small due to the low concentration of the microwires (Fig. 11.17a). Nevertheless, a dependence of $\varepsilon'$ on the applied magnetic field is demonstrated. The transformation of resonance to relaxation can be inferred from the frequency evolution of these curves. The anisotropy field can be used as a critical value to distinguish the frequency dependence of $\varepsilon'$ at the studied frequency range (1–5 GHz). The same trend is also observed in the frequency plots of $\varepsilon''$ (Fig. 11.17b). This is explained as follows. When $H_{ex} < H_k$, the impedance is increased with $H_{ex}$. Therefore, the internal loss increases and the relaxation dispersion occurs. The relaxation behaviour is fully achieved when $H_{ex} = H_k$, whereby the impedance reaches a maximum. Further increase of Hex results in a reverse trend. Note that the dielectric response to the

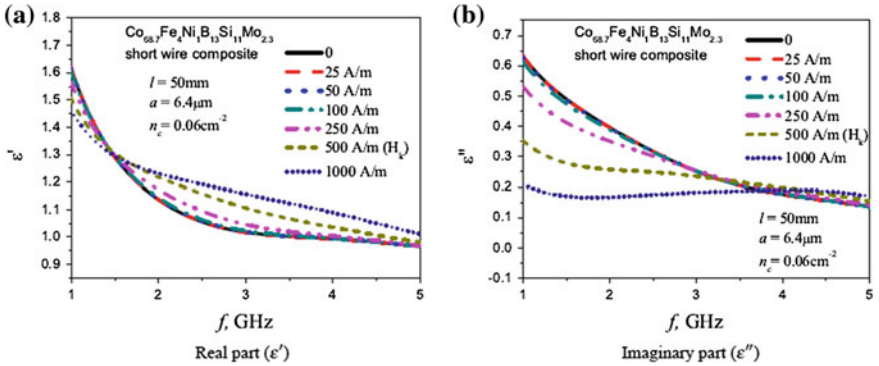


**Fig. 11.17** Effective permittivity spectra of a short-wire composite with varying magnetic field relative to anisotropy field (500 A/m). The material parameters are given in the graph: $l$ is the wire length, $a$ is the wire radius, $n_c$ is the ratio of wire number to the area containing them. Reprinted with permission from [69], copyright 2013 Elsevier

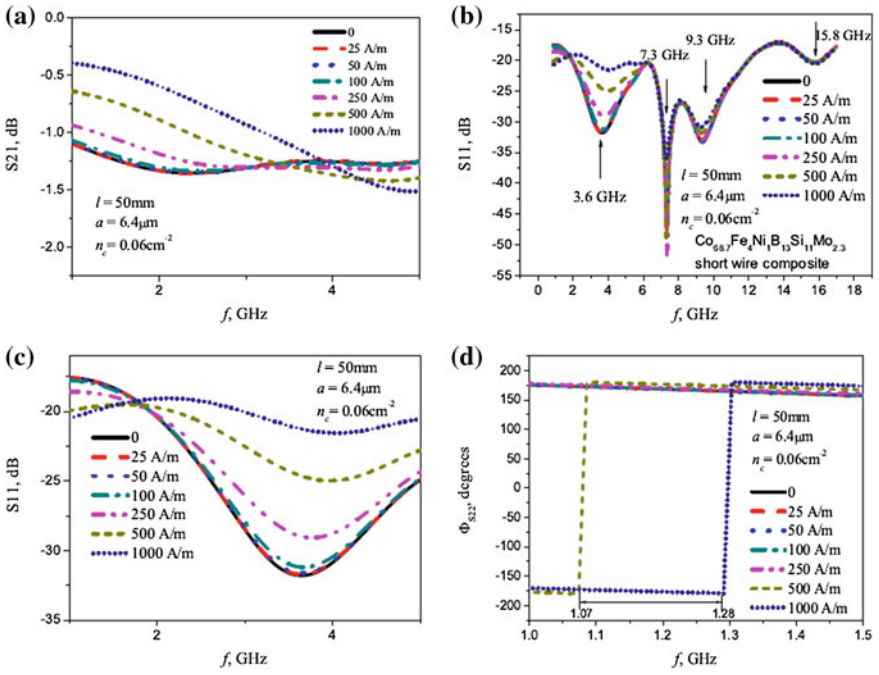


**Fig. 11.18** **a** Transmission and **b** reflection spectra of a short-wire composite with the magnetic field as a parameter; **c** part of (**b**) at 1–5 GHz; **d** the phase of reflection coefficient. The phase reversal shift is indicated in the graph with coordinate values given. The material parameters are given in the graph by the same symbols as in Fig. 11.17. Reprinted with permission from [69], copyright 2013 Elsevier

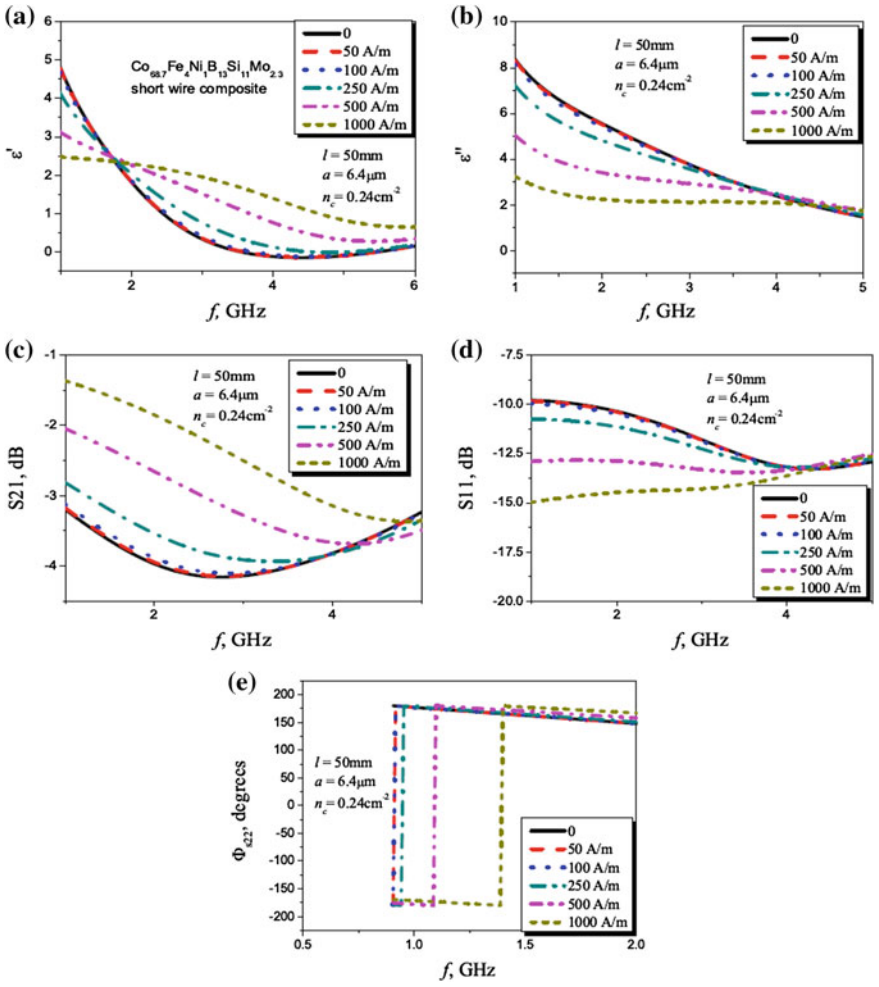


**Fig. 11.19** Experimental dispersion of **a** real and **b** imaginary part of effective permittivity; **c** measured transmission and **d** reflection spectra of the short-wire composite with the magnetic field as a parameter; **e** presents the phase of reflection coefficient. The material parameters are given in the graph by the same symbols as in Fig. 11.17. Reprinted with permission from [69], copyright 2013 Elsevier

magnetic field is not seen until the field reaches 250 A/m; this is likely due to the relative insensitivity of magnetoimpedance for this range of magnetic field.

As with the complex permittivity spectra, the transmission is increased as the field increases, with a concomitant resonance/relaxation change, as seen in Fig. 11.18a. Strikingly, the transmission spectra present a large transmission of *ca.* 90 %, which corresponds to a very large return loss (see Fig. 11.18b). With the same spectra zoomed at 1–5 GHz (Fig. 11.18c), the resonance/relaxation

transformation is clearly observed with increasing magnetic field. The resonance/relaxation frequency shifts to a higher value with increasing magnetic field. The phase shift Φ is also shown in the reflection spectra, as depicted in Fig. 11.18d.

By decreasing the wire periodicity from 20 to 5 mm, the area concentration of wires is greatly increased from 0.06 to 0.24 $cm^{-2}$. As a result, the values of the measured *S*-parameters are largely increased while their field dependences remain unchanged (Fig. 11.19a–d). Inasmuch as the wire geometry (length, diameter and aspect ratio) remains unchanged, there will not be significant changes in the dispersion behaviour as far as the composite mesostructure is concerned. It should be noted that, although the phase shift remains unchanged when the field increases from 500 to 1000 A/m, a reduction from 500 to 100 A/m is found to cause a phase reversal between $-\pi$ and $\pi$ in the reflection spectra (Fig. 11.19e).

## 11.4 High Field Tunable Properties

The high field effect that we aim to study here refers to the magnetic field of the order of 100–1000 Oe, which is in contrast to the low magnetic field of no more than 50 Oe. In this section, we will treat the effective permittivity of different kinds of microwire composites by a modified frequency-domain spectroscopy and reveal intriguing physics behind some unique phenomena such as the crossover field and double peak exhibited in the permittivity spectra.

### *11.4.1 High Field Dependence of Permittivity*

Two kinds of samples containing Co-based melt-extracted microwires are used for microwave characterisation, i.e. continuous-wire samples and random-wire samples. For the random-wire sample, 50 mg of 5-mm-long wires were randomly dispersed in a silicone rubber by mechanical mixing. The mixture was subsequently mould-casted to obtain samples with dimensions 70 × 10 × 1.8 $mm^3$ and cured at ambient temperature for 24 h (Fig. 11.20a). The resultant sample has a microwire content of 3 wt%. For continuous-wire samples, 70-mm-long microwires were aligned in a periodical manner (Fig. 11.20b) with fixed wire spacing of 0.77 mm into silicon rubber matrix sheets which were bonded together using silicone resin.

Representative spectra of the real, $\varepsilon'$, and imaginary, $\varepsilon''$, parts of the complex permittivity at five different magnetic bias values for sample A are shown in Fig. 11.21. At zero magnetic field, the permittivity shows a relaxation behaviour. When a magnetic field of 100 Oe is applied, $\varepsilon'$ is found to increase and the relaxation remains visible. With further increase of the magnetic field up to 500 Oe, an absorption peak is seen near 4.1 GHz (Fig. 11.21b). This maximum shifts to higher frequencies of, respectively, 4.6 and 4.7 GHz as the magnetic field is

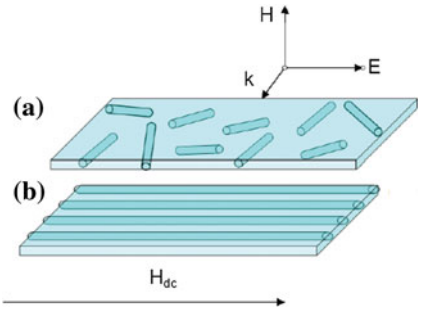


**Fig. 11.20** **a** Schematic illustration of random-wire sample. **b** Same as in (**a**) for continuous-wire sample. The electric field vector of the electromagnetic wave is parallel to the wire axis. The applied magnetic field $H_{dc}$ is directed along the wire axis. Reprinted with permission from [23], copyright 2012 AIP

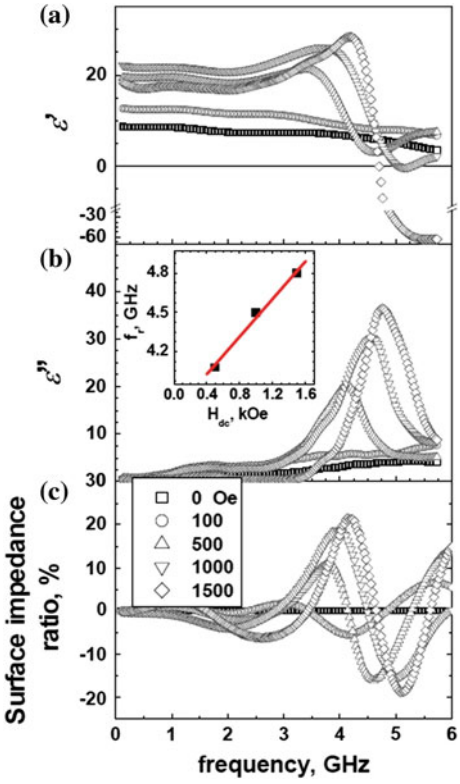


**Fig. 11.21** **a** Frequency dependence of the real part of the effective permittivity for random-wire sample at varying magnetic fields. **b** Same as in (**a**) for the imaginary part of the effective permittivity; the inset shows the field dependence of magnetoimpedance resonance extracted from (**b**). **c** Frequency dependence of the surface impedance ratio at varying magnetic fields. Reprinted with permission from [23], copyright 2012 AIP

increased to 1 and 1.5 kOe, with increased height and width. The peak is associated with anomalous dispersion of Fig. 11.21a, leading to negative values of $\varepsilon'$ for frequencies higher than 4.7 GHz for magnetic fields over 1 kOe.

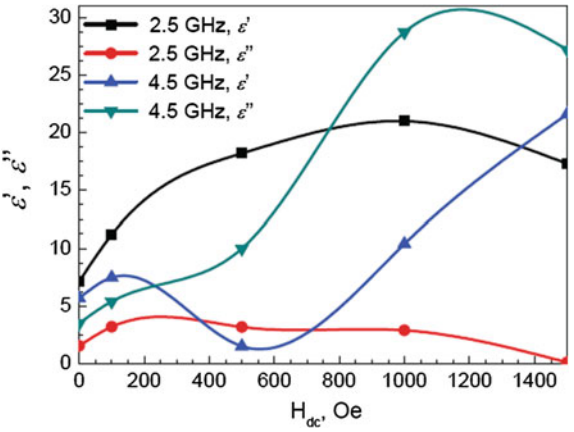


**Fig. 11.22** Magnetic field dependence of the real and imaginary parts of the effective complex permittivity for random-wire sample at 2.5 and 4.5 GHz. Reprinted with permission from [23], copyright 2012 AIP

Figure 11.22 presents the magnetic bias dependence of the real and imaginary parts of the effective complex permittivity for the random-wire sample at 2.5 and 4.5 GHz. At 2.5 GHz (off resonance), the variations in and $\varepsilon''$ are small. This contrasts with the rather pronounced changes of $\varepsilon'$ and $\varepsilon''$ observed at 4.5 GHz (resonance). It can also be seen that, at 4.5 GHz, the application of a magnetic field excitation gives rise to an $\varepsilon''$ larger than $\varepsilon'$, which is not seen at 2.5 GHz.

In order to examine the influence of the magnetic bias on the permittivity of the continuous-wire sample, we turn now to analysing the microwave absorptive behaviour probed by our electromagnetic measurements (Fig. 11.23). Two well-separated absorption lines are found in the ranges 1–2 and 4–5 GHz, respectively. Note that the bias dependence of permittivity can be clearly observed for each

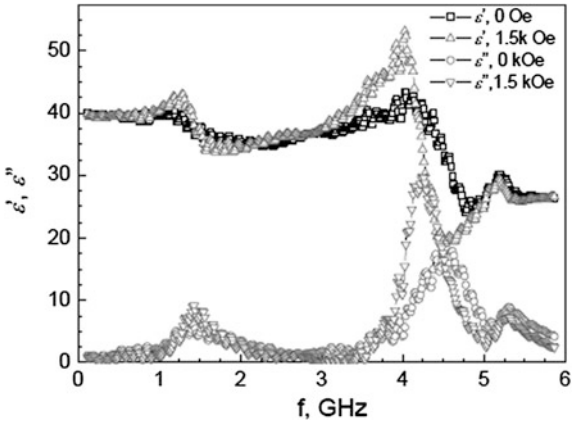


**Fig. 11.23** Frequency dependence of the real and imaginary parts of the effective complex permittivity for continuous-wire sample at zero magnetic field and 1.5 kOe. Reprinted with permission from [23], copyright 2012 AIP

resonance region. As the magnetic field is increased, the absorption line at 4–5 GHz grows in magnitude and becomes narrower. The linewidths of the dielectric and magnetoimpedance resonances present opposite variations as the field is increased.

Two aspects of the above results should be noted. The first is that microwires respond to the electromagnetic wave like electric dipoles for sample A. The dipole resonance can be expressed as $f_{\text{res}} = c/2l\sqrt{\varepsilon_m}$ [11], where $c$ is the electromagnetic wave velocity in vacuum, $l$ is the wire length, and $\varepsilon_m$ is the permittivity of the host matrix. When $l$ is chosen at 5 mm, the resonance frequency is close to 15 GHz, which is out of the measurement range of the present work. This explains the absence of the absorption line in the spectrum without, or with low applied magnetic field. With the application of high magnetic field, our results demonstrate that the current induces resonance of circumferential permeability; that is, the magnetoimpedance resonance results in a significant change of the effective permittivity of the wire-filled composites [24, 25, 73]. Since the applied magnetic field strongly influences the current distribution in the microwires through the skin effect, this gives rise to a significant change of the dielectric response in the GHz range of frequencies. As the magnetoimpedance resonance frequency is below the dielectric resonance frequency, absorption within the skin effect predominates over dipolar absorption and has the effect of increasing the absorption linewidth [24]. The blueshift of resonance frequency with the field $H_{dc}$ (cf. the inset of Fig. 11.21b) is consistent with the field effect on the surface impedance profiles calculated from $S$-parameters, as shown in Fig. 11.21c. The interest in the microwave behaviour of these composite samples lies also partly in its anomalous dispersion [74]. Since application of a magnetic bias can lead to large eddy current losses, we suggest that wire-filled composites can be exploited for designing microwave absorbers having a large absorption bandwidth. In addition, the anomalous dispersion is often associated with a negative value of $\varepsilon'$. Thus, a variety of unusual properties can be engineered to meet the requirements of a high-performance frequency selective surface. It should be noted that while the magnetic bias has a strong influence on the permittivity, it has a negligible effect on the magnetic permeability (not shown here). Since the wire concentration is low, the magnetic permeability is close to unity in the GHz range of frequencies. For sample B, the wires which are perpendicular to the microwave magnetic field do not contribute, whereas those which are parallel have no response to the field in the GHz range of frequencies. Hence, we predict that the sensitivity of permittivity to frequency and magnetic field will result in useful applications of this kind of microwire composite samples.

The second point deals specifically with the continuous-wire sample. Compared with the random-wire sample, it is notable that it has a much lower dipole resonance frequency at 1.1 GHz according to $f_{\text{res}} = c/2l\sqrt{\varepsilon_m}$, which is in good agreement with the lower-frequency peak shown in Fig. 11.22. The difference observed with the experimental value of the resonance frequency can be attributed to interfacial defects in the composite, e.g. imperfect bonding.

To summarise, we have evaluated in this section the microwave response of composite samples containing glass-covered amorphous microwires embedded in a

rubber matrix with different wire lengths and topological arrangements. The obtained results show that there is a strong dependence of the permittivity spectra on the external magnetic bias. For wire composites containing randomly dispersed wires of 5 mm length, the real part of the permittivity increases as the magnetic bias is increased until it attains a maximum which corresponds to the maximum absorption induced by the magnetoimpedance resonance. The absorption resonance frequency and linewidth can be conveniently tuned by the magnetic bias. Composites containing periodically arranged longer wires (70 mm) are characterised by a double-resonance permittivity spectrum. The higher-frequency resonance is associated with magnetoimpedance resonance. It has a narrower linewidth than that of the lower-frequency (dipole) resonance as the magnetic field is increased. The assessment of the high field effect points to interesting physics in our understanding of the electromagnetic properties of composite materials with tunable microwave properties at very high magnetic fields.

### *11.4.2 Crossover Phenomenon*

In the present and next section, we will discuss some unusual phenomena observed in the microwave spectra of the microwire composites in the presence of high magnetic fields. Understanding the physics behind these peculiar observations provides insights into the structure–property relationship of the microwire composites. Thus, we can optimise the design of the composite architecture and, in another perspective, exploit the usefulness of microwave characterisation techniques as a research tool to probe the materials' micron or even nanostructure.

The crossover phenomenon we deal with in this section refers to the existence of a critical field dividing a reverse field effect on the electromagnetic parameters below and above. The phenomenon was observed in a set of epoxy-based microwire composites containing 25-mm Co-based glass-coated microwires randomly dispersed as shown in Fig. 11.24 and submitted to an external magnetic field from 0 to 1 kOe.

Figure 11.25 compares the zero-field transmission, reflection, and permittivity spectra for three microwire weight fractions. The observed difference in the frequency dependence of these quantities is not surprising. Two features can be noticed. Firstly, a large increase of $\varepsilon'$ and $\varepsilon''$ is observed with increasing contents of microwires; the most prominent feature in Fig. 11.25c is the peak in the $\varepsilon''$ spectra, which is related to a dipolar resonance phenomenon. While the peak positions do


**Fig. 11.24** Image of the composite sample containing 0.026 vol% microwires. Reprinted with permission from [75], copyright 2012 AIP

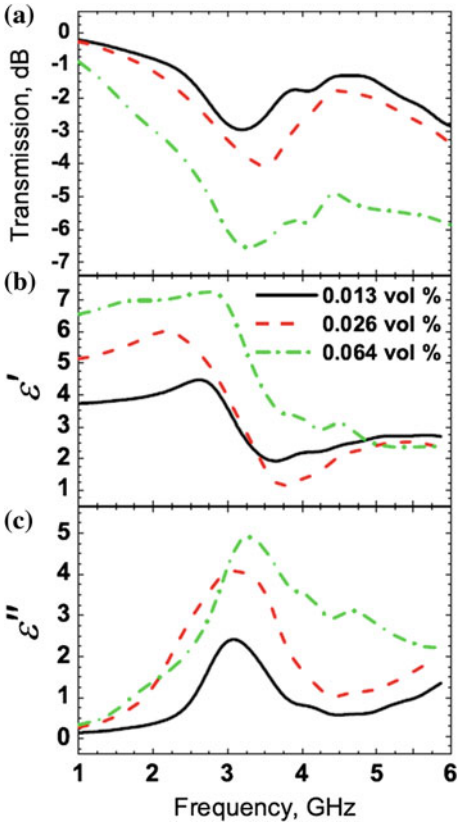


**Fig. 11.25** The transmission spectra (**a**), frequency dispersion of the real, $\varepsilon'$, (**b**) and imaginary parts, $\varepsilon''$, **c** of the effective complex permittivity for microwire/epoxy composites with varying concentration. Reprinted with permission from [75], copyright 2012 AIP

not significantly shift with wire concentration, the peak size and width increase strongly with wire content. The dipolar resonance frequency is calculated to be 3.2 GHz, which is close to the peak positions observed in Fig. 11.25c. The differences in peak height and width between the three wire weight fractions are probably related to the microwire content. Secondly, a minimum of transmission is observed close to the resonance position.

In Fig. 11.26, the field dependence of the electromagnetic parameters for the sample containing 0.013 vol% of microwires is plotted as a function of frequency at low magnetic field (up to 300 Oe). First, we note the contrasting behaviour of the transmission and reflection coefficients as the magnetic field is increased, as seen in Fig. 11.26a and c, respectively. Further, the reflection maximum or transmission minimum corresponding to the resonance frequency is redshifted with increase of the magnetic field. For a quantitative analysis, we fitted the *H*-dependent resonance position with a linear function and plotted it in Fig. 11.26c. We exhibit in Fig. 11.27 the corresponding spectra at higher fields (between 300 Oe and 1 kOe). In all cases, we observe opposing field-dependent behaviour of the electromagnetic parameters. That is, the reflection spectra increase in magnitude, whereas the corresponding

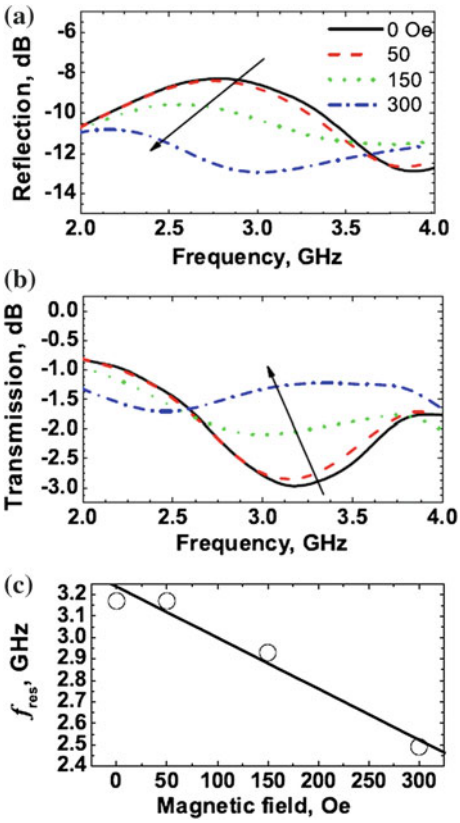


**Fig. 11.26** The transmission spectra (**a**), reflection spectra (**b**), and field dependence of resonance frequency (**c**) under a dc field of 0–300 Oe. The sample contains 0.013 vol% microwires. The solid line in (**c**) is a linear fit to the data. Reprinted with permission from [75], copyright 2012 AIP

transmission spectra decrease. We note that this contrasting behaviour has not been predicted previously. For other composite samples containing different microwire concentrations, the field crossover at 300 Oe was also evident (Fig. 11.28). Interestingly, we observe that the magnitude of the transmission and reflection spectra at 300 Oe of the composite samples is quite similar for the different microwire concentrations investigated. Together, these observations support the conclusion that the linear variation of the resonance position shift against the magnetic field is an intrinsic property of the microwires in the samples.

One can think of this crossover at 300 Oe as arising from a competition between the two resonant phenomena characterising this system. As was seen earlier, the first resonance is the dipole resonance (3.2 GHz). The second resonance phenomenon is associated with the ferromagnetic resonance (2.3 GHz), which is in close proximity to the dipole one. Specifically, when the ferromagnetic resonance occurs to the microwire at sufficiently high magnetic fields, the skin depth reaches a minimum and hence gives rise to a maximum dielectric loss. As is now well established, the Co-based amorphous wires possess remarkable GMI properties. In the GHz range of frequencies, the GMI effect 1 dominates the features of dipolar

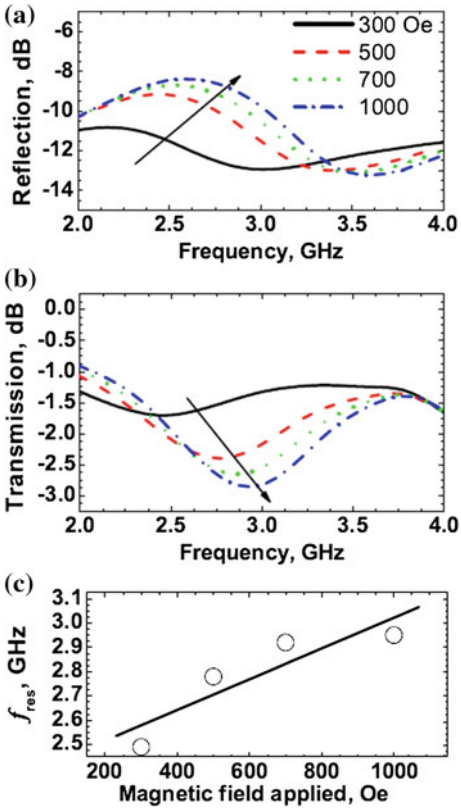


**Fig. 11.27** Same as in Fig. 11.26 for the dc magnetic field in the range 300–1000 Oe. Reprinted with permission from [75], copyright 2012 AIP

absorption at low magnetic field bias. As the magnetic field is increased, the impedance increases. Hence, the permittivity together with the reflection and absorption is decreased. Consequently, the transmission is increased, as seen in Figs. 11.26b, 11.28a and c. This is also consistent with what was observed in free-space characterisation of short-cut microwire composites [72]. Now, if the magnitude of the magnetic field is larger than 300 Oe, we hypothesise that the electromagnetic characteristics are dominated by the FMR. As the magnetic field is increased, losses are enhanced. This is reminiscent of the eddy current in the microwires at FMR. Although the penetration depth at 2.4 GHz falls between 1 and 2 μm, microwaves can still penetrate the outer layer of the wire and result in eddy current loss [76]. Several reasons may contribute to the actual value of the crossover field at 300 Oe. For instance, we notice that the GMI effect requires relatively small magnetic field magnitudes, while the FMR is driven by a stronger field. This is consistent with the experimental results and the insensitivity of the crossover field against microwire content.

We now briefly turn to the magnetic field tunability of the effective permittivity of the samples. In Fig. 11.29, the quantities shown are the ratios $[\varepsilon'(H) - \varepsilon'(H = 0)]/\varepsilon'(H = 0)$ and $[\varepsilon''(H) - \varepsilon''(H = 0)]/\varepsilon''(H = 0)$, where different curves denote

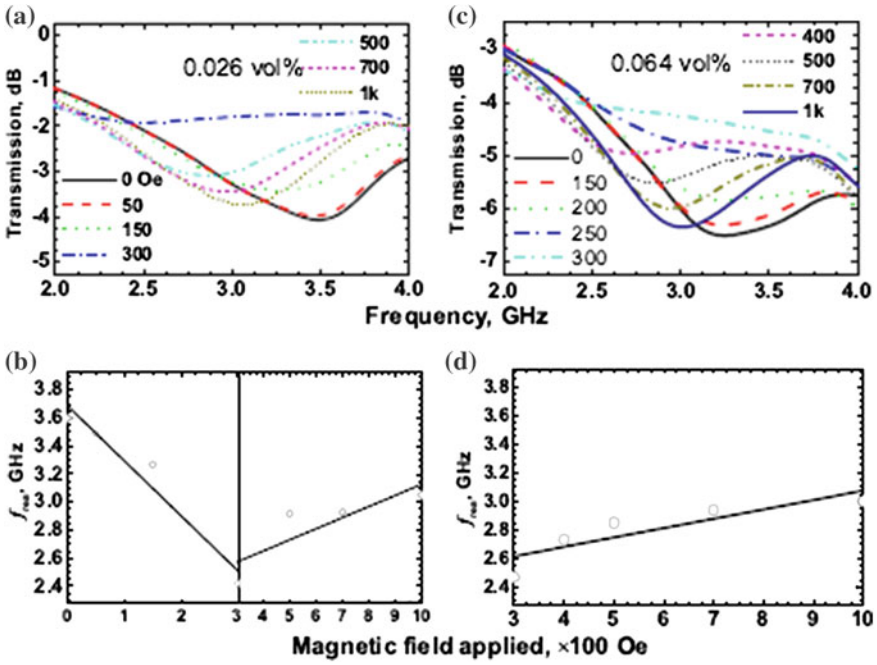


**Fig. 11.28** **a** The transmission spectra for the sample containing 0.026 vol% microwires and different dc magnetic field excitations in the range 0–1 kOe. **b** The resonance frequency plotted as a function of the applied magnetic field. The *solid lines* are linear fits to the data. Notice the change in the slope of these lines at ≈300 Oe. **c** Same as in (**a**) for the sample containing 0.064 vol% microwires. **d** Same as in (**b**) for the sample containing 0.064 vol% microwires. Reprinted with permission from [75], copyright 2012 AIP

the different frequencies. Figure 11.28 shows a detailed comparison of these quantities for the three microwire contents. Overall, one can clearly see a peak feature at 300 Oe and the magnitude of this peak observed in these data can be as high as 150 % for 2.4 GHz, i.e. close to the FMR. Surprisingly, however, both Fig. 11.29c–d show that the larger effect is observed for the sample containing 0.2 wt% of microwires. We present a simple explanation for this behaviour. One expects that a large amount of microwire will improve the field-induced polarisation properties of the sample. Hence, the reflection and transmission coefficients and the value of the effective permittivity increase when the wire concentration increases from 0.013 to 0.026 vol%. Both magnetic and dielectric losses are enhanced, and consequently the overall absorption is also increased in agreement with previous measurements [77, 78]. However, the reflection losses also increase with microwire content. If these losses are too high, they will prevent efficient tuning of the microwire composites. This observation supports that low-loaded composites are required for efficient tunability. One might expect the maximum at 0.026 vol%

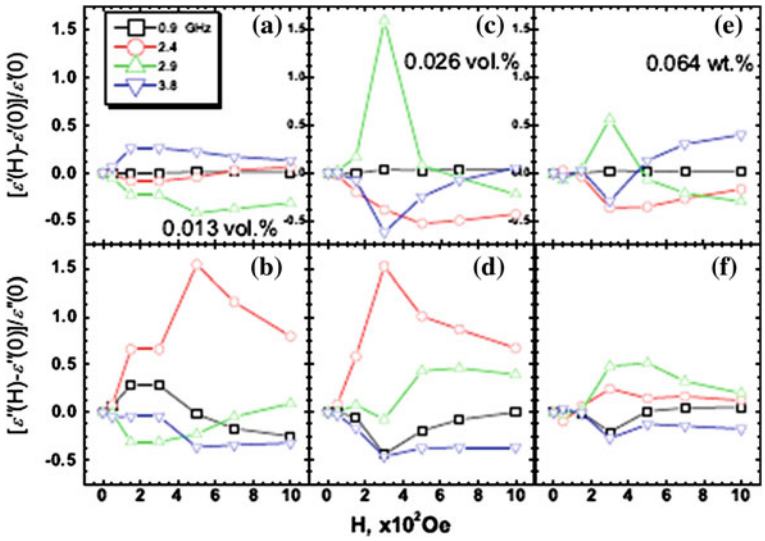


**Fig. 11.29** **a** The magnetic field dependence of $[\varepsilon'(H) - \varepsilon'(H = 0)]/\varepsilon'(H = 0)$ at different frequencies for the sample containing 0.013 vol% microwires. **b** Same as in (**a**) for $[\varepsilon''(H) - \varepsilon''(H = 0)]/\varepsilon''(H = 0)$. **c** Same as in (**a**) for the sample containing 0.026 vol% microwires. **d** Same as in (**b**) for the sample containing 0.026 vol% microwires. **e** Same as in (**a**) for the sample containing 0.064 vol% microwires. **f** Same as in (**b**) for the sample containing 0.064 vol% microwires. Reprinted with permission from [75], copyright 2012AIP

to vary according to the microwires aspect ratio and intrinsic properties, and also fabrication protocol.

As a summary of this section, the crossover phenomenon has been identified via the investigation of the electromagnetic parameters of glass-covered amorphous microwires/epoxy composites with various concentrations of microwires over a broad magnetic field range up to 1 kOe. The results presented here show that the effective permittivity presents a strong tunability with respect to a dc magnetic field excitation. An inherent crossover field due to the microwires is further observed at 300 Oe. This observation can be understood intuitively by considering that the GMI effect dominates the features of dipolar absorption at low magnetic field bias (<300 Oe), while the opposite behaviour is expected at larger dc magnetic field excitations. We also point out that this crossover field is insensitive to changes in the microwire content. The largest magnetic field tunability of the effective permittivity of the samples is found at the microwire content of 0.026 vol%. These conclusions add strong impetus for designing glass-covered amorphous microwires/epoxy composites as adaptive materials for reconfigurable electronic devices and sensing applications, for which manipulation of the dielectric properties via a magnetic field excitation can be accomplished. It is also worth mentioning that the latest results obtained from our laboratory show that this crossover effect can also be found in the Fe-based microwire composites.

### 11.4.3 Double-Peak Phenomenon

The double-peak phenomenon has been found in the composites containing melt-extracted microwires. We present this unique case to demonstrate the versatility of the microwave behaviour of the microwire composites. Also, since microwire composites are primarily advantageous in their electromagnetic functionalities at microwave frequency, which are partially attributed to the soft magnetic properties of wires, characterisation of these with the aid of high field will give us a better understanding of the structure and the properties of wires. This suggests that the microwire composites can serve as a valuable medium to study the microwires.

The primary results of this section are shown in Figs. 11.30 and 11.31, which plot the effective complex permittivity spectra for the continuous-wire composite sample with, respectively, 6 and 8 wires and for field magnitudes from 0 to 1 kOe. Prominent in the data are the two pronounced and broad absorption peaks at 2.6 and 4.2 GHz. The peak at 2.6 GHz is much broader than the one at 4.2 GHz. Interestingly, there are some substantial differences between the behaviour of the two peaks when a magnetic field is applied. The magnitude of the $\varepsilon''$ peak at 2.6 GHz increases by a factor of 2 and its full-width half-maximum (FWHM) is significantly reduced when the magnetic field is increased from 0 to 1 kOe. The line shape and intensity of the peak at 4.2 GHz exhibit little change as a function of magnetic field; however, increasing magnetic field produces a visible redshift.

The comparison of Figs. 11.30 and 11.31 is instructive. We find that the value of $\varepsilon''$ for the peak at 2.6 GHz for the sample with 8 wires is significantly smaller than the corresponding peak for the sample with 6 wires, while the opposite trend is shown at the second peak of 4.2 GHz. The relative importance of the field effect

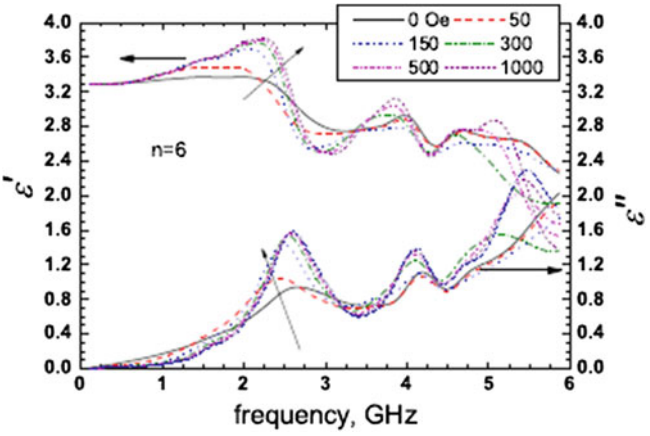


**Fig. 11.30** The $\varepsilon'$ and $\varepsilon''$ spectra for the sample containing 6 wires and for magnetic field magnitudes from 0 to 1 kOe. Reprinted with permission from [79], copyright 2013 AIP

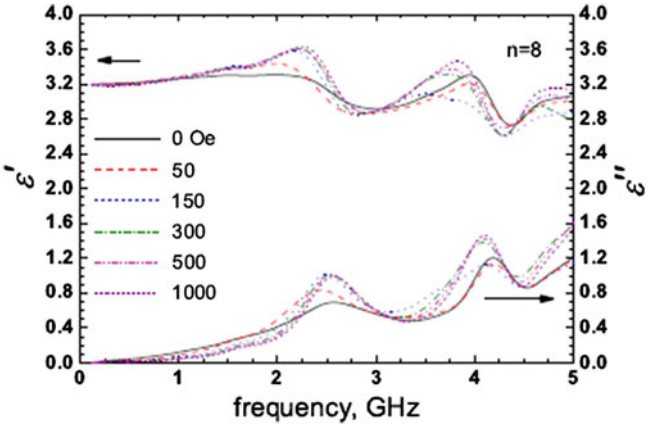


**Fig. 11.31** Same as in Fig. 11.30 for the sample containing 8 wires. Reprinted with permission from [79], copyright 2013 AIP

from 150 Oe onwards in varying the permittivity is much larger at the first resonance for the $n = 6$ sample than the $n = 8$ one, while little change appears at the second resonance. The two-peak feature of the dielectric losses evidenced in Figs. 11.30 and 11.31 warrants further discussion. As noted in the previous sections, the ferromagnetic resonance (FMR) mode is intrinsic to the ferromagnetic microwires. When no external static magnetic field is applied, the FMR depends on the saturation magnetisation $M_s$ and anisotropy field $H_k$ of the microwires, expressed as $f_{\mathrm{FMR}} = \gamma = (M_s + H_k/2\pi)$, where $\gamma$ is the gyromagnetic ratio [80]. For amorphous microwires with a small anisotropy field $(H_k \ll 2\pi M_s)$, one can write $f_{\mathrm{FMR}} \approx \gamma 2\pi M_s$. Taking $M_s$ = 850 G, $f_{\mathrm{FMR}}$ = 2.4 GHz, which is in close correspondence to the value of 2.6 GHz observed experimentally. This small discrepancy can be attributed to the complex internal stress distribution appearing in the microwires during the rapid cooling rate, leading to a non-uniform distribution of local magnetoelastic anisotropy. When a magnetic field is applied, the relative importance of stress is weakened and the FMR mode is blueshifted as the field is increased, according to Kittel's law. The electromagnetic response of homogenised grids of parallel amorphous ferromagnetic microwires has been studied recently by Liberal et al. [81] by using the local field method and the transmission-line analogy. Following these authors, the reduction of the skin depth as the magnetic field is increased could provide an explanation for the increase of permittivity at the first peak observed in Figs. 11.30 and 11.31.

The resonance peak at 4.2 GHz can be distinguished from the FMR mode by examining the dependence of the dielectric losses versus the magnetic field. To put this into perspective, we assume that the microwires have a core-shell (CS) structure, i.e. a core amorphous phase surrounded by a nanocrystalline shell, and we consider that the nanocrystalline phase is responsible for the resonance peak at 4.2 GHz. HRTEM is a unique analytical tool for such study because it

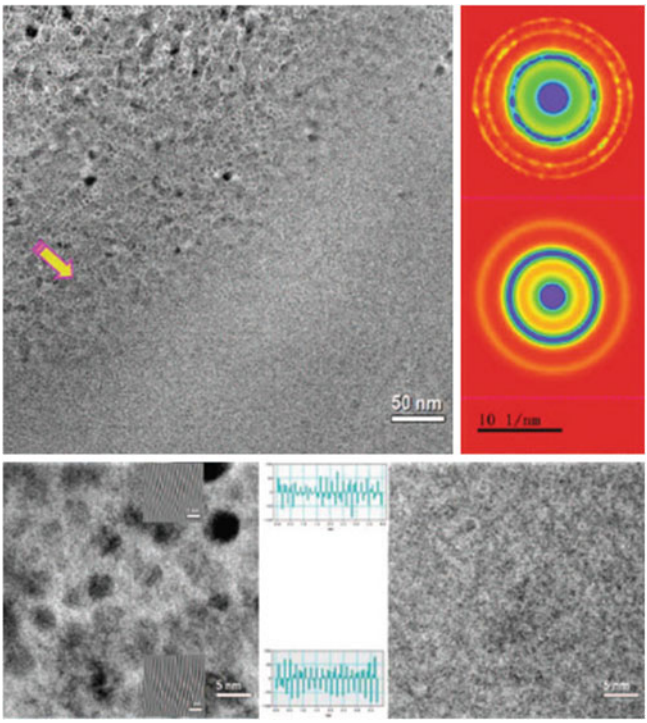


**Fig. 11.32** HRTEM images and SAED of the studied microwire, and the corresponding local magnifications. **a** HRTEM images of biphasic structure of microwires, including nanocrystalline region I, amorphous region II and transition region III; The unidirectional arrow indicates the radial direction of the microwire. **b** SAEDs of biphasic structure, marked by *blue rectangles* (as shown in 1 and 2, respectively) in (**a**); the upper I is polycrystalline rings (consisting of CoFe, CoSi, and Co2B) SAED of rectangle 1 and the lower II is halo ring SAED of rectangle 2. **c** Local magnifications (rectangles 3 and 4) and their corresponding IFFT patterns and the estimative interplanar distances (D3 and D4) of nanocrystalline structure; **d** Local magnification of amorphous structure of rectangle 2 in (**a**). Reprinted with permission from [79], copyright 2013 AIP

can provide high-resolution microstructural and well as electron diffraction data. As shown in Fig. 11.32a, the nanocrystalline phase, amorphous phase split by a transition region, is clearly identified along the radial direction from the surface to the inner core. The polycrystalline rings representing the nanocrystalline phase and the halo ring representing the amorphous phase are also readily present in the selective area electronic diffraction (SAED) images (Fig. 11.32b). Further observations of the magnified nanocrystalline region and amorphous region were displayed in Fig. 11.32c and d, respectively. The nanocrystallites average 2 nm. The formation of nanocrystallites is attributed to the melt extraction process [82]. As schematically shown in Fig. 11.33, in the first stage, heat transferred rapidly and unidirectionally from the thin layer to the copper wheel, and the resulting

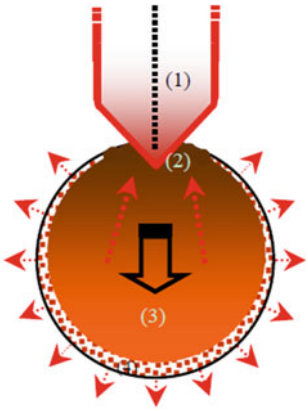


**Fig. 11.33** Proposed schematic model illustrating the formation of nanocrystalline phase in the melt extraction process. The numbers in the graphs have the following denotations: (*1*) indicates the copper wheel; (*2*) indicates the connection area between the copper wheel and melt drop; (*3*) and (*4*) label the amorphous and nanocrystalline phase, respectively. The *red up arrows* and *circular array of arrows* indicate the heat conduction and radiation, respectively. The *black down arrow* refers to the uniaxial solidification. Reprinted with permission from [79], copyright 2013 AIP

inhomogeneities from the non-uniform chemistry and stress distribution can thus act as nucleation sites for nanocrystallites in the subsequent solidification process. In the second stage, the heat energy dissipation changes from heat exchange to much-slower thermal radiation, which facilitates the precipitation of nanocrystallites on the top layer of the free surface. A similar phase separation in melt-extracted FeCuSiB microwires has been reported by Nagase and Umakoshi [83]. We would like to stress that the thin glass-coated wires fabricated by the Taylor–Ulitovskiy method do not show a two-peak structure of the absorption losses. This is due to the absence of such crystalline phase because glass-coated wires are generally too thin to give the slow cooling rate which is of paramount importance for nanocrystallite formation. Note that this could explain why the thin wires fabricated by the Taylor–Ulitovskiy method have much better magnetic softness and associated GMI properties than melt extraction microwires [84].

The existence of nanocrystallites is also evidenced in the microwave characterisation. The first peak is broader than the second one, in that the above-mentioned strong non-uniform distribution of magnetoelastic anisotropy contributes multiple resonance frequencies which merge into a broad one. In this sense, the minor fraction of nanocrystalline phase shows a much narrower resonance. In addition, the Co nanocrystalline phase is much magnetically harder than the amorphous phase, which results in the negligible field effect (<150 Oe) in the low magnetic field, and even the high magnetic field (>150 Oe) is only adequate to improve the resistance but not sufficient to tune the resonance frequency. With increasing wire concentration, the magnetic shielding effect predominates over the

increasing polarisation with more wires [85], which results in the reduction of the first peak and the diminished field effect accordingly. While the nanocrystalline phase does not respond very well to the external field, the increasing concentration predominates over the shielding effect and results in an increase of permittivity.

In the following, we are going to check whether our experimental data are consistent with a two-phase CS modelling. First, we consider that the intrinsic permittivity of the microwires can be written as $\varepsilon_i = \beta\varepsilon_m^{\text{amor}} + (1-\beta)\varepsilon_m^{\text{nano}}$, where $\beta$ is a relative weight of the amorphous phase with respect to the nanocrystalline phase. Here, $\varepsilon_m^{\text{nano}}$ and $\varepsilon_m^{\text{amor}}$, respectively, represent the shell and core contributions to the intrinsic permittivity of the microwires. The Drude–Lorentz model is applied here to model the effective permittivity; that is, $\varepsilon'' m$ can be written in the form $\varepsilon'' m = A_k(f/f_k)[\left(1-\left(f/f_{0,k}\right)^2\right)^2 + \left(f/f_{r,k}\right)^2]$, where the $A_k$s are resonance peak amplitudes, $f$ denotes the frequency of the wave, $f_{r,k}$ is the resonance frequency of the $k$th peak, and $f_{0,k}$ is related to the width of the $k$th resonance line. A simple model of the effective permittivity of our samples in the long-wavelength limit is to use an arithmetic mean of the intrinsic permittivity of the phases weighted by their respective volume fractions. Inspection of Fig. 11.34 shows a good agreement between the fit and data. Residual discrepancy observed may be due to imperfect bonding between the rubber and the microwires and uncertainty in our $\varepsilon_i$ value.

Finally, we examine the influence of frequency in the three zones of Fig. 11.32 within the context of the CS structure of the microwires. In Fig. 11.35, we plot the Cole-Cole representation of the permittivity data for the sample containing 6 wires. The observed behaviour is complicated and could be described by three zones. On the one hand, it is apparent from Fig. 11.34 that several relaxation mechanisms contribute to the permittivity spectra shown in Figs. 11.30 and 11.31. On the other hand, ferromagnetic/rubber composites enable the optimisation of the field-induced tunability of the effective permittivity, as we can simultaneously vary $\varepsilon''$ and $\varepsilon'$ in a controlled manner. One intuitive explanation for the three zones would be to consider that they are associated with, respectively, the amorphous and crystalline phases, and the amorphous to crystalline phase interface. We find that the change in the effective permittivity due to the magnetic perturbation is a sensitive indicator of dielectric relaxation and resonance mechanisms. As to the purely amorphous region, GMI is predominant at low magnetic bias, while FMR is important at high bias, as discussed in the preceding section. Another relaxation process can be related to the amorphous to crystalline phase interface. While at low magnetic field excitation the amorphous phase contributes significantly to the dielectric response, an increasing magnetic bias tends to increase the importance of the crystalline phase of this microwave response. The relaxation associated with the crystalline phase requires the involvement of a high magnetic field.

In summary, in this section, we have evaluated the features associated with the two-peak behaviour of the permittivity spectra for ferromagnetic microwire/rubber composites in the 0.3–6 GHz range of frequencies. We have investigated how these spectra vary with magnetic field and the number of microwires inside the sample. We argue that this spectral feature may be attributed to the amorphous

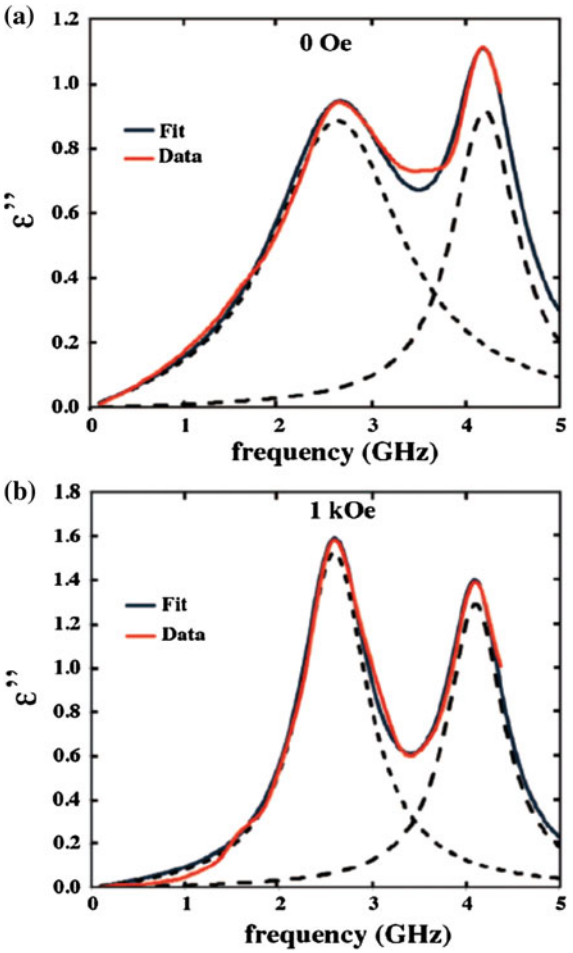


**Fig. 11.34** Simulated $\varepsilon''$ spectra for the structure containing 6 wires and two values of the magnetic field amplitudes (0 and 1 kOe). The *solid line* is a fit to the data for an amorphous core-crystalline shell model with 0.15 vol%. Reprinted with permission from [79], copyright 2013 AIP

core-crystalline nanoshell structure of the microwires. Electromagnetic simulations show that the Drude–Lorentz model of dispersion can describe satisfactorily the effective permittivity in the range of frequencies explored. Based on the analyses of HRTEM images and the microwave spectra, the microwave characterisation using frequency-domain spectroscopy can be exploited for express detection of the minor fraction of nanocrystallites formed in the surface of materials.

Before closing the whole section dealing with the high field effect, we would like to comment that although a strong field may not be desirable in practice, since most applications desire to be free from cumbersome magnets, they are useful to reveal some special functionalities and associated physics that would otherwise be obscured in natural conditions. From a practical point of view, they can be exploited as facile but effective research tools to study the materials structure. Above all, the physics underlying the high field effect may also extend the possibilities of

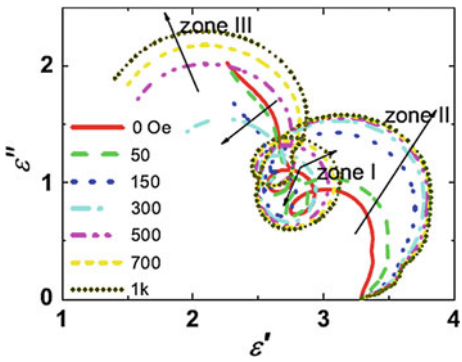


**Fig. 11.35** The Cole–Cole representation of the data in Fig. 11.30 for the sample containing 6 wires. Three zones are identified as the magnetic field magnitude is varied from 0 to 1 kOe. The evolution of each zone as the magnetic field is increased is indicated by the *arrows*. Reprinted with permission from [79], copyright 2013 AIP

optimising the microwire composite structure and broaden its functionalities and applications.

## 11.5 Stress Tunable Properties

Due to the stress effect on the impedance of amorphous wires, the stress will have a significant impact on the prorogation of microwaves when they pass through the microwire(s). This is characterised by the variation of electromagnetic parameters (reflection, transmission, permittivity, and permeability) with stress. This is the basic working principle for microwave NDT methods [86–92]. Compared to other NDT methods, employing ultrasound [93, 94], infrared thermography [94–96], radiography [97, 98], radioactive computed tomography, and ground-penetrating radar (GPR) [99, 100], microwave proves to be advantageous due to the fact that microwaves can penetrate deep inside the composite, scatter little compared to acoustic waves, offer excellent contrast between matrix and reinforcing fibres, have good resolution, are not hazardous, are cost-effective compared to radioactive methods, and are robust to environmental conditions unlike infrared methods [86–92]. Both near-field [101, 102] and far-field free-space [86] characterisations of composite structure have proved to be useful in detecting the debonds and delaminations of composite structure, demonstrating the usefulness of microwave NDT technology in structural health monitoring applications. However, without embedding sensors, it is hard to detect the local damage. Most recently, the potential of using carbon fibres themselves as antennae and sensors to precisely detect the damage in CFRP has also been demonstrated [103]. However, the interactions of CFRP and microwaves are limited by the high conduction loss of CF due to the high volume fraction. The use of microwires as sensor elements is

advantageous for their strong interactions with microwaves and high sensitivity to external fields. In what follows, we will discuss the stress effect on the wire impedance and the stress tunable effects of microwire composites at gigahertz frequencies.

### *11.5.1 Stress Sensing Based on Microwires*

The stress influence of GMI or stress-impedance effect has been mostly discussed in the megahertz frequencies due to the application interest [104–110]. Interested readers are kindly referred to [44, 66, 67] and the references therein. The focus here is on the stress effect of GMI behaviour in the gigahertz frequency.

At gigahertz frequencies, the skin effect is very strong with a small skin depth (e.g. around 1.2 μm at 1–10 GHz) [11]. The permeability is contributed by the outer layer of the microwire. For Co-based microwire with the circumferential domain structure in the outer layer, the permeability is determined by the natural ferromagnetic resonance [47]. According to the Landau–Lifshitz–Gilbert (LLG) equation, the permeability is strongly dependent on the anisotropy field of the wires. Considering the significant stress impact on the anisotropy field of wires [12, 62, 111–113] and anisotropy angle [10, 15, 49], the permeability (or impedance) spectra can be regulated by the variation of internal stress due to that of geometry [113–116] or glass removal [117], and external stress [21] as shown in Fig. 11.36a. The resonance frequency can be regulated by the parameter of the microwires and the number of wires. Therefore, this effect could be utilised, beyond stress sensing, for detecting and locating damage in the microwire-based composites [103], which is of much interest in engineering applications. In Fig. 11.36b and c, the sensing resolution is obtained from the shift of resonance with stress/strain with values of 1.06 MHz/MPa and 134.5 kHz/microstrain, respectively. These results lead to an important revelation that the microwires can be used as stress sensors in a wide frequency range, provided the permeability can be obtained. Compared with the newly proposed SRR-based sensor with a sensitivity of 5.148 kHz/microstrain [118], the microwires are much more cost-effective and possess a higher Q factor and sensitivity. The susceptibility of permeability to stress can be tailored either by tuning the composition, geometry, and microstructure of the microwires [113], or through developing composites containing magnetic fillers [119] and non-magnetic fillers [120].

It is worth mentioning that the stress sensitivity of impedance for single wires can be modulated by the dc bias field. When the external magnetic field is equal to the value of the anisotropy field, the stress sensitivity reaches a maximum. This is demonstrated in Fig. 11.37 [121], where the maximum sensitivity is shown at 15 Oe. The reason for this is well explained by the dependence of permeability on the anisotropy angle, formulated as [49]:

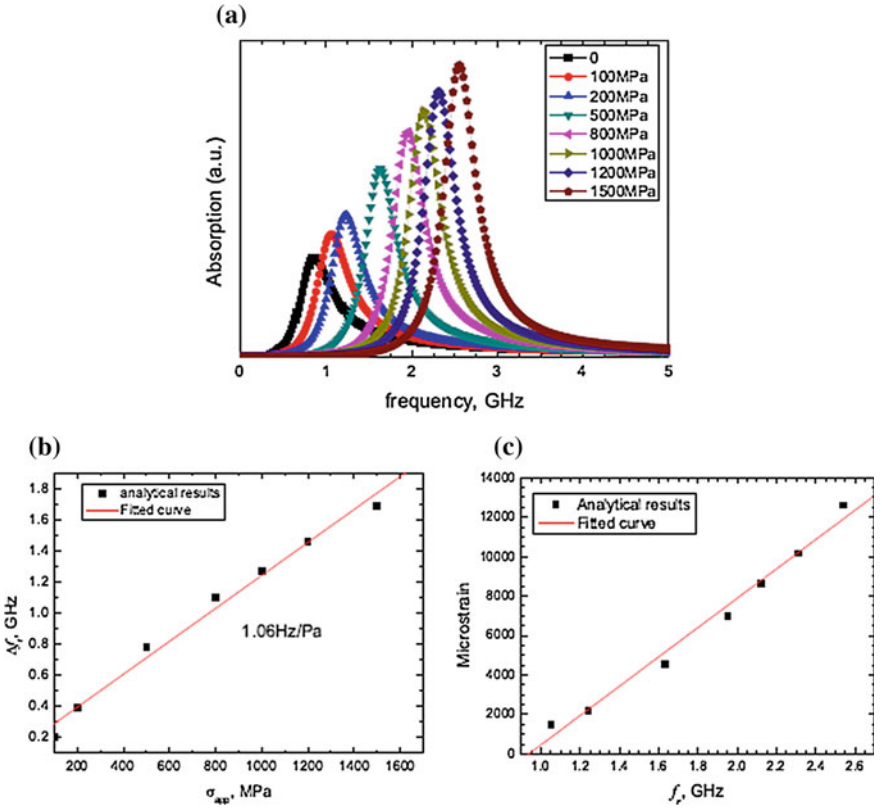


**Fig. 11.36** **a** Calculated absorption spectra under varying $\sigma_{\text{app}}$ according to LLG formula $\mu = 1 + \frac{\mu_0\gamma M_s[\mu_0\gamma(H_{dc}+H_k)-j\omega\alpha]}{-\omega^2+\omega_{\text{FMR}}^2-j\omega\alpha\mu_0\gamma[2(H_{dc}+H_k)+M_s]}$, and $H_k = \frac{3|\lambda_s|}{M_s}(\sigma_{zz} - \sigma_{\phi\phi} + \sigma_{\text{app}})$ with the material parameters obtained from magnetisation test: $M_s = 10^6 \sim \text{A/m}$, $\gamma = 2.21 \times 10^5\ \text{mA}^{-1}\text{s}^{-1}$, $\alpha = 0.02$, $H_s = 880 \sim \text{A/m}$ and $\mu_0 = 1$. **b** Applied stress dependence of resonance frequency shift. The slope of fitted line represents the stress-sensing resolution. **c** Resonance frequency dependence of microstrain. The slope of *fitted line* represents the strain-sensing resolution. Reprinted with permission from [21], copyright 2010 Elsevier

$$\mu = 1 + 4\pi\cos^2(\theta). \tag{11.17}$$

The application of magnetic field along the wire axis increases the circumferential magnetic permeability by rotating the magnetisation vector towards the wire axis. On the other hand, when a stress is applied along the microwires with a negative magnetostriction, the magnetisation vector rotates away from the axis direction. As a result, the circumferential magnetic permeability is decreased [10]. It is expected, therefore, that the application of longitudinal stress will compensate the effect of the magnetic field. The influence of stress is more obvious with a high magnetic field. Indeed, with reference to Fig. 11.37, the maximum applied stress of

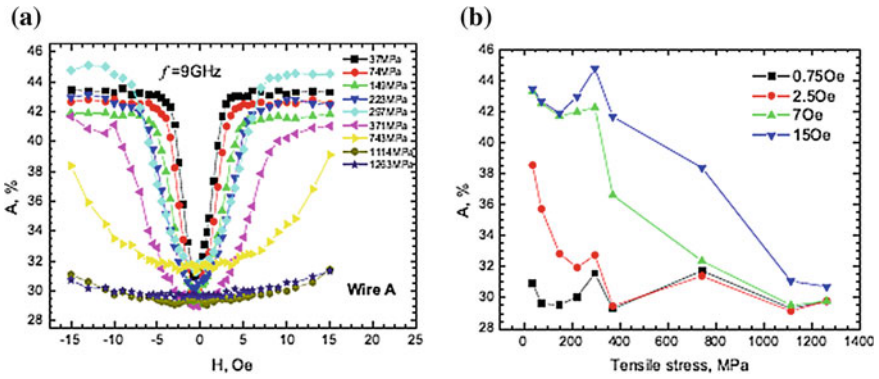


**Fig. 11.37** **a** Axial field dependence of absorption in the presence of varying stress at 9 GHz for a $Co_{67}Fe_{3.9}Ni_{1.4}B_{11.5}Si_{14.5}Mo_{1.7}$ wire of total diameter 30.6 μm and glass coat 5.2 μm. **b** Tensile stress dependence of absorption (impedance) at varying magnetic fields for the same wire. Reprinted with permission from [121], copyright 2011 Elsevier

1263 MPa encourages the absorption back to the original value by offsetting the effects of the magnetic field. The magnetic field along the wire axis is desirable for the absorption of microwires and can also be utilised to increase the stress sensitivity of absorption. Similar results were also reported in [10, 15]. Upon analysing the data in Fig. 11.37, it can be obtained that the sensitivity of absorption to stress increases by ca. 39 times when the field increases from 0.75 to 15 Oe. This has profound implication in designing wire-based stress sensors.

## *11.5.2 Stress Tunable Properties of Composites*

### 11.5.2.1 Stress Tunable Properties of Composites in Free Space

Figure 11.38 [27] shows the complex permittivity spectra for as-prepared intact rubber-based composite prepared by the method described in Sect. 9.2.3 and after being damaged with the occurrence of wire breakage. There are pronounced changes for both the real part $\varepsilon'$ and the imaginary part $\varepsilon''$ of effective permittivity. In particular, a drastic change of $\varepsilon'$ is seen with a reversal of sign from negative to positive when the wire breakage happened to the composite in question.

For the composites containing $Fe_{4.84}Co_{56.51}B_{14.16}Si_{11.41}Cr_{13.08}$, there is no response at all for the composite subjected to a load range from 0 to 4 kg (not shown here). However, a stress tunable behaviour parallel to the field tunable behaviour is observed in the transmission spectra (Fig. 11.39). Interestingly, the composite shows a similar response to stress and magnetic field, although the evolution of transmission with magnetic field is steadier than that with stress. To gain a deeper insight into such stress tunable characteristics, Fig. 11.40 is plotted to

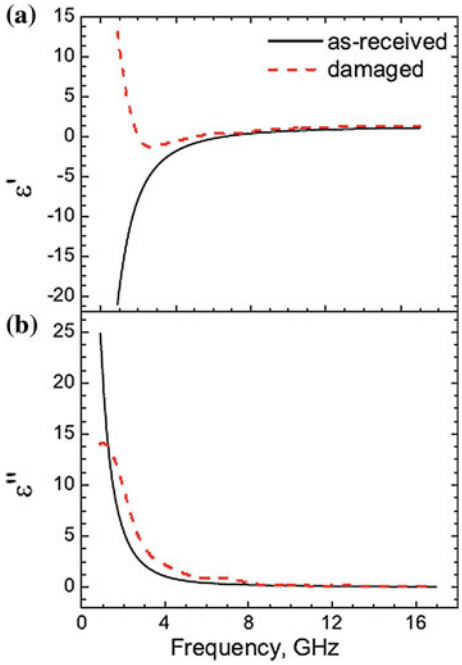


**Fig. 11.38** Complex permittivity spectra of as-received composite and after damage by tensile stress. Reprinted with permission from [27], copyright 2011 AIP

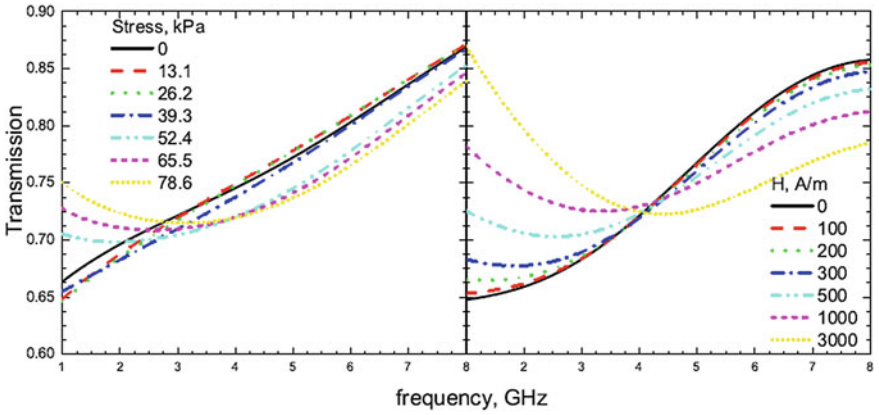


**Fig. 11.39** Effect of stress (*left*) and magnetic filed (*right*) on transmission spectra of microwire composite containing $Fe_4Co_{68.7}Ni_1B_{13}Si_{11}Mo_{2.3}$ microwires. Reprinted with permission from [27], copyright 2011 AIP

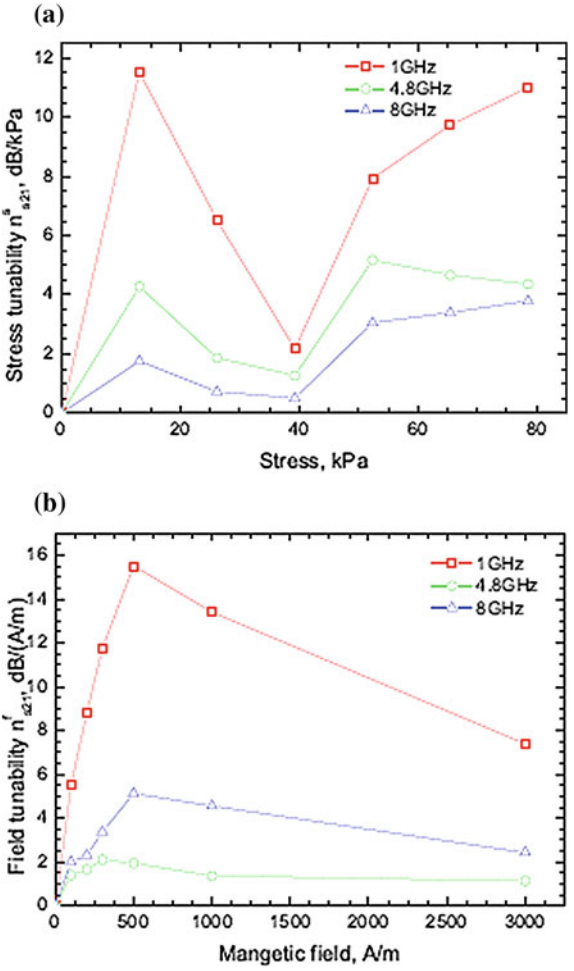


**Fig. 11.40** **a** Stress and **b** field dependence of tunability at 1, 4.8, and 8 GHz, plasma frequency $f_p$ = 4.8 GHz, the ordinate profiles are normalised by $10^{-4}$ and $10^{-5}$, respectively. Reprinted with permission from [27], copyright 2011 AIP

show the calculated stress (resp. magnetic field) tunability versus stress (resp. magnetic field) at 1, 4.8, and 8 GHz, which are lower, equal, and higher in relative to the plasma frequency ($f_p$), respectively. The overall evolution of tunability remains the same trend at all three frequencies. In comparison with the single peak feature displayed in the magnetic field dependence of tenability (Fig. 11.40b), both a maximum and a minimum appeared in the stress dependence of tunability.

The primary principle pertinent to the stress tunable phenomenon is as follows. For composite containing ferromagnetic wires exhibiting a giant magnetoimpedance effect at microwave frequencies, the effective permittivity may depend on a dc magnetic field via the corresponding dependence of the surface impedance. The surface impedance can also be changed by applying a stress which modifies the magnetic anisotropy and domain structure in the wires. Thus, the effective

permittivity may also depend on the external stress or strain. It follows that the stress-impedance (SI) property of microwires is critical to the susceptibility of the whole composite to the stress. SI depends strongly on the magnetoelastic characteristics of the microwire, which are conditioned by a number of factors: composition, domain structure, geometry, etc. This accounts for the observed insensitivity and sensitivity of the microwire composites in terms of their permittivity to the external stress when dealing with different wires. Although all these amorphous wires can be expected to show a drastic change when breakage occurs in the composite, the choicest wires have to be evaluated when it comes to a more delicate stress-sensing application.

The single peak presented in the stress tunability of $S_{21}$ ($n^f_{s_{21}}(H)$) is associated with the anisotropy field. By contrast, a more complex relationship of $n^f_{s_{21}}(\sigma)$ merits more discussion. It is well established that the Co-based microwires with a negative magnetostriction have a bamboo-like domain structure, consisting of an inner core and an outer shell [44]. The surface impedance depends on the circumferential anisotropy at the outer shell. When a stress is applied along the axis of a microwire with negative magnetostriction, a magnetoelastic field is induced in the circumferential direction and this drives the spins rotating towards that direction. As a result, the circumferential magnetic permeability is decreased, and hence, the surface impedance is also reduced. It is expected, therefore, that the application of a longitudinal stress will compensate the effect of the magnetic field. This explains the maximum that occurred at around 13 kPa (Fig. 11.40a). Afterwards, with increasing stress, the well-defined circumferential anisotropy may remain unchanged and hence the surface impedance shows very little variation to the incremental stress, giving rise to a minimum of tenability at 40 kPa. Larger stress than 40 kPa may depreciate the circumferential anisotropy and increase the surface magnetoimpedance, which accounts for the recovery of the increased tunability with stress. It should be noted that tens of kPa imposed on the composite yields hundreds of MPa on each wire, according to a simple calculation as follows. As the present case meets the isostrain condition, the following equation holds:

$$\varepsilon = \frac{\sigma_c}{E_c} = \varepsilon_w = \frac{\sigma_w}{E_w}, \tag{11.18}$$

where $\varepsilon_c$ and $\varepsilon_w$ denote the strain for composite and microwires, respectively; $\sigma_c$ and $\sigma_w$ the stress exerted on the composite and microwires, respectively; $E_c$ and $E_w$ the Young's modulus of the composite and microwires, respectively. Using the law of mixture, the stress each microwire experiences is given by

$$\sigma_w = \frac{\sigma_c}{\left(\frac{E_m}{E_w}\right) f_m + f_w}, \tag{11.19}$$

where $f_m$ and $f_w$ are the volume fraction of the matrix and microwires, respectively. Due to the significant difference between the Young's modulus of rubber matrix

(2 MPa) and of microwires (100 GPa), 10 kPa on the composite can result in 500 MPa on the microwires. This is within the reasonable stress range as commonly discussed in literature, in terms of the stress effect on GMI properties of microwires (see, e.g. [13, 62]).

#### 11.5.2.2 Stress Influence of Electromagnetic Properties Measured by Spectroscopy

For composite containing ferromagnetic wires exhibiting a giant magnetoimpedance effect at microwave frequencies, the effective permittivity may depend on a dc magnetic field via the corresponding dependence of the surface impedance. The surface impedance can be changed by applying a stress which modifies the magnetic anisotropy and domain structure in wires. Thus, the effective permittivity may also depend on the external stress or strain. Following the stress tunable theory proposed by Panina et al. [9], Qin et al. [32, 122] approached the strain effect on the electromagnetic responses from the technological aspects of the multifunctional composites: $Co_{56.51}Fe_{4.84}B_{14.16}Si_{11.41}Cr_{13.08}$ glass-covered magnetic microwires having a total diameter of 29.4 mm and silicone rubber were used for the preparation of composite materials. Continuous microwires with the same length of 70 mm were embedded in a parallel manner into the silicone rubber matrices, which were bonded by silicone resin (see Sect. 9.2.3 for further details). The number ($n$) of the microwires in composites varied with $n$ = 6, 12, and 17 corresponding to the wire spacing $d$ = 2, 1, and 0.8 mm. For comparison, copper wires with a diameter of 60 mm were also used as fillers. The resultant composites are of uniform dimension of 70 mm × 13 mm × 1.8 mm.

The electromagnetic measurement was carried out with a wave vector of the electromagnetic field perpendicular to the wires using a modified microwave frequency-domain spectroscopy within the frequency range between 300 MHz and 5 GHz. Details of the instruments were discussed in Sect. 11.2.2. All measurements were done at ambient temperature.

Figure 11.41 shows the permittivity spectra for composites containing different amounts of microwires and 12 copper wires. For the unstressed sample, the real component of permittivity $\varepsilon'$ increases with the wire amount. For the same amount of wires, composite containing copper wires displays a larger $\varepsilon'$ than that with ferromagnetic microwires. The same trend remains when the strain reaches 2.4 % as the tensile stress is applied along the longitudinal direction of the composite. Noticeably, there appears a broad relaxation peak at about 4 GHz for the $n$ = 12 sample when $\lambda$ = 2.4 % and, with the same strain, a sharper peak occurs at around the same frequency for the $n$ = 17 sample. A similar evolution of permittivity spectra with strain is also shown in the imaginary component ($\varepsilon''$). But such a phenomenon is not observed for the $n$ = 6 sample and the sample with copper wires. It is also interesting to note that $\varepsilon''$ of the sample with copper wires is smaller than those with magnetic microwires.

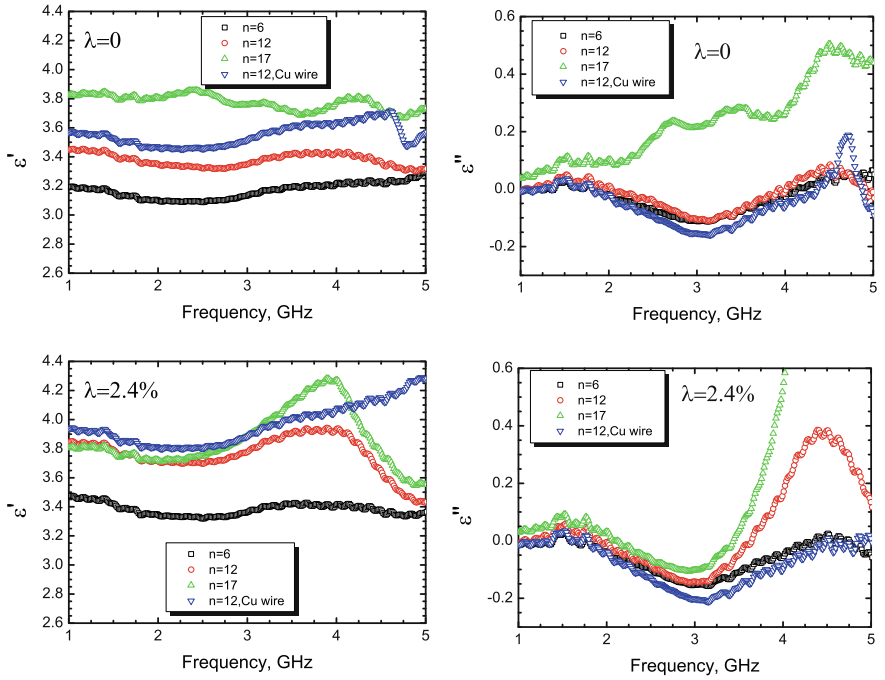


**Fig. 11.41** Effective complex permittivity spectra for unstressed composites ($\lambda = 0$) and stressed composites with 2.4 % strain containing varying amounts of microwires. Reprinted with permission from [69], copyright 2013 Elsevier

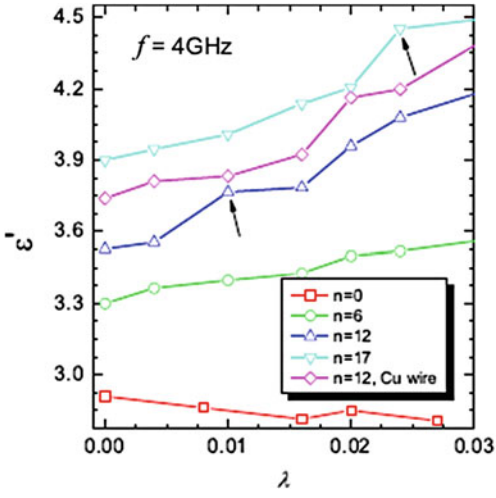


**Fig. 11.42** Strain dependence of $\varepsilon'$ for composites with $n$ as a variable. Reprinted with permission from [69], copyright 2013 Elsevier

Figure 11.42 summarises the strain dependence of $\varepsilon'$. The sample without wires shows the expected response of $\varepsilon'$ to stress. After adding fillers into the composite, its $\varepsilon'$ starts to show relatively stronger stress sensitivity, which increases with the

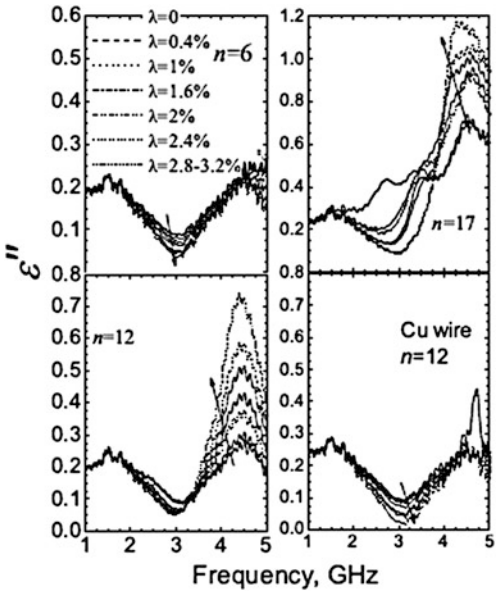


**Fig. 11.43** Spectra of $\varepsilon''$ for composites containing ferromagnetic microwires $n$ = 6, 12, 17, and 12 copper wires with strain $\lambda$ as a parameter. Reprinted with permission from [69], copyright 2013 Elsevier

amount of wire. The sample with copper wires presents a similar stress sensitivity of $\varepsilon'$ to that containing the same amount of magnetic microwires. Figure 11.43 summarises the $\varepsilon''$ spectra for all samples, with strain ranging from zero to 2.8–3.2 %. Note that the strain values discussed herein are nominal. Overall, there is a significant influence of the microwire amount on $\varepsilon''$. The strain effects also vary with the wire amount. For the $n$ = 6 sample, $\varepsilon''$ is almost independent of the strain. For the $n$ = 12 sample, there is a remarkable dependence of $\varepsilon''$ on strain, featured as the evolution of a symmetric resonance peak at 4.5 GHz. As $n$ increases to 17, the peak position and the evolution trend with the strain remain unchanged, but the shape becomes asymmetric. In contrast, the sample with the copper wires exhibits a complex evolution of the resonance peak with the strain, such that the resonance peak occurring at the unstressed state increases with a small strain of 2 % but disappears at larger strains. To exclude the influence of geometrical factors of the composites 0 and the microwires, Fig. 11.44 was plotted to show the frequency dependence of tan $\delta$ (ratio of $\varepsilon''$ to $\varepsilon'$), and the evolution of peak features with strain remains the same trend as in Fig. 11.43.

The strain dependence of effective permittivity is quantitatively analysed by the Gaussian molecular network model (GMNM) [42]. Figure 11.45 shows the $\lambda$ dependence of $\Delta$ with varying amounts of wires, where $\Delta = (\varepsilon'(\lambda) - \varepsilon'(\lambda = 0)/\varepsilon'(\lambda = 0)$. This relationship is well fitted by a functional form $k(1 + \lambda - 1/(1 + \lambda)^2)$, where $k$ is a constant, the value of which varies with the wire amount as shown in Fig. 11.45.

The effective permittivity ($\varepsilon$) is dependent on the wire concentration ($p_v$) and the averaged polarisability ($\langle a \rangle$): $\varepsilon = \varepsilon_m + 4\pi p_v \langle a \rangle$, where $\varepsilon_m$ denotes the permittivity of

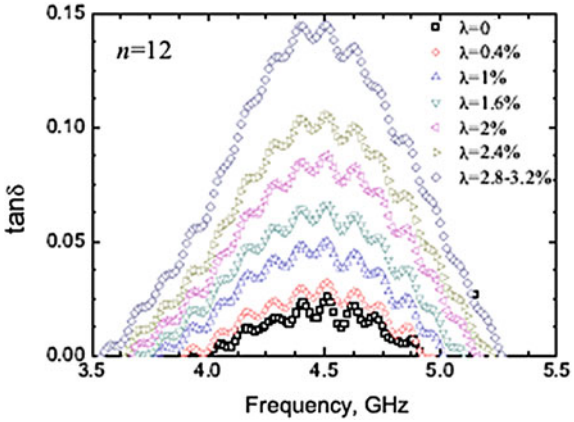


**Fig. 11.44** Frequency dependence of loss tangent with strain as a parameter. Reprinted with permission from [32], copyright 2010 AIP

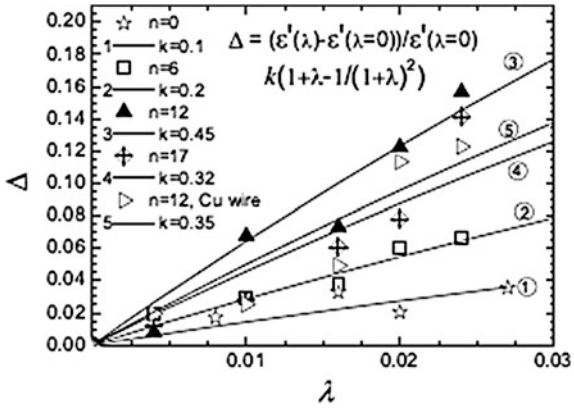


**Fig. 11.45** Variations of Δ with strain for composites with differing amount of wires as shown in the *open symbols* at 4 GHz. The best *fitted lines* to the function of $k(1 + \lambda - 1/(1 + \lambda)^2)$ and values of $k$ corresponding to different n are also shown. Reprinted with permission from [32], copyright 2010 AIP

matrix [9]. Thus, increasing the wire amount improves the effective polarisation and hence the permittivity. The polarisability is primarily dependent on electric excitation. For the present composite configuration with microwires perpendicular to the electric field vector, although the sample is aligned with the tensile axis of the deformation apparatus, an axial component of electrical field still exists due to the inevitable misalignment of the wires within the sample and/or the possible inhomogeneity of the electrical field in the cell, which may affect the electric excitation of the wires. This accounts for the observed dielectric response of the composite

samples due to the polarisation and the induced circumferential magnetisation of the wires. For the magnetic microwires, the strain modifies the magnetisation process and hence the circumferential permeability, resulting in the changes of $\varepsilon'$. However, since the experimental data were obtained using the same protocol and measurement cell, the changes of permittivity can be solely attributed to strain.

It is also shown that more microwires induce a sharper peak at ca. 4 GHz, indicating an increased stress sensitivity. However, this argument does not hold true for the composites with $n = 6$ and copper wires which can be understood as follows: for $n = 6$, the wires concentration is not high enough to satisfy the response of a noticeable peak to the external stress; for copper wires, they have no response to the induced circumferential magnetic field, and therefore, the composite does not show any stress-induced peaks. Overall, the effective permittivity of wire composites increases with the strain, which is further discussed later based on the GMNM approach. It is worth pointing out that, owing to the higher concentration of copper wires as a result of larger diameter than that of ferromagnetic microwires, the composite sample with copper wires shows a larger permittivity than that with the same amount of ferromagnetic microwires.

From the application point of view, it is important to find ways to improve the stress sensitivity. Obviously, this can be approached by increasing the amount of microwires in the composite. However, it should be noted that this does not necessarily mean that more is better. In this work, the sensitivity of permittivity to stress showed little change between the $n = 12$ and $n = 17$ samples. Somewhat surprisingly, it is found that the samples containing magnetic microwires and containing non-magnetic microwires appear to yield a similar stress sensitivity of $\varepsilon''$. This observation suggests an independence of the stress sensitivity in wire composites to the conductivity and magnetic permeability of the wires for a sufficiently high concentration of wires, although the reason for this result is not obvious.

The most striking feature shown in Fig. 11.43 is the evolution of the peak with the stress for the n = 12 and $n = 17$ samples. It is proposed that the gradual spectral change from relaxation to resonance at 4.5 GHz can also be attributed to the influence of stress on wire magnetisation, as discussed above, which modifies the eddy current loss and contributes to the steady evolution of the $\varepsilon''$ resonance due to the circumferential ferromagnetic resonance.

The loss tangent (tan $\delta$) retains the same changing trend with the strain as $\varepsilon''$ ($\lambda$), indicating that such a strain effect is independent of any geometrical factors [123]. It should be noted that such a transformation of relaxation to resonance is absent for the $n = 6$ sample and composite with copper wires in the spectra of complex permittivity. This suggests the exclusivity of ferromagnetic microwires and the requirement of the wire concentration to realise a steady evolution of the peak feature defined by the stress [24].

Now we discuss the strain–permittivity relationship. Basically, the GMNM approach is related to the elasticity network of the composite material. Excellent agreement between the experimental results and the GMNM model is observed for

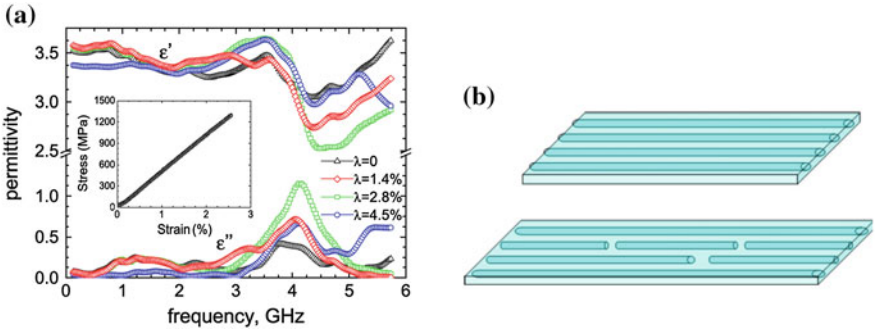


**Fig. 11.46** Spectra of complex permittivity for microwire composites with strain $\lambda$

all samples (Fig. 11.45), which suggests the applicability of the model at the measured strain range. By introducing more microwires ($n \leq 12$) into the rubber matrix, a higher stress sensitivity (characterised by the $k$ value in this case) and a closer experimental–model match is obtained. But when $n$ increases to 17, $k$ is decreased and a relatively larger mismatch is observed. This can be attributed to the enhanced complexity of the composite mesostructure, arising from the larger amount of embedded microwires [42]. Nevertheless, due to the periodical topology of the microwires within the composite, GMNM gives fairly good predictions for all samples.

The significance of wire patterns is manifested in Fig. 11.46a, in which a non-linear dependence of $\varepsilon''$ on the strain is shown. In this case, the wire starts to snap when the strain exceeds 2.8 %. Due to the uneven interfacial properties, each single wire may experience a different stress, which results in partial but not total fracture of all wires. We then receive a similar resonance response for two patterns (Fig. 11.46b). This indicates that the increase of dielectric loss with the stress is compensated with the opposite effect resulting from the reduction of strained wires. There are two possible mechanisms involved in this phenomenon. First is the stress effect: the stress changes the current distribution in the wires and induces higher dielectric loss, and release of stress results in the opposite effect. Second is the shape effect: the wires are fractured to relatively shorter pieces and the anisotropy field of the wire becomes non-uniform and results in the reduction and broadening of the resonance linewidth. This leads us to a striking revelation in a larger context, that the functional fillers enabled heterogeneous composites, the macroscopic behaviour is dependent on the collective response of the fillers on the one hand, and each single filler on the other hand. This then poses the challenge of how to manipulate some, if not each, of the fillers. In so doing, we will have greater control of the properties of the composite presented to meet specific applications.

## 11.6 Temperature Tunable Properties

By analogy with stress, the temperature tunable properties are derived from the temperature dependence of GMI properties. Because the magnetic permeability is sensitive to temperature, the GMI changes rapidly as a function of temperature, especially in the vicinity of the Curie temperature $T_c$. In general, for Co-based microwires, the GMI effect first increases with increase of the measuring temperature due to the internal stress relief, reaches a maximum value near the Curie temperature of the material, and then finally decreases at higher temperatures [124, 125]. The dramatic change of GMI at temperatures above the Curie point was attributed to the collapse of the magnetic coupling in the material [126], which has been exploited for the development of temperature sensors [127]. In terms of composites, the magnetic phase transition at $T_c$ will lead to a large transformation of the dispersion of effective permittivity, as well as the reflection and transmission coefficients [18]. Figure 11.47 shows the theoretical permittivity spectra and transmission/reflection spectra for $T < T_c$ and $T > T_c$. By analogy with the influence

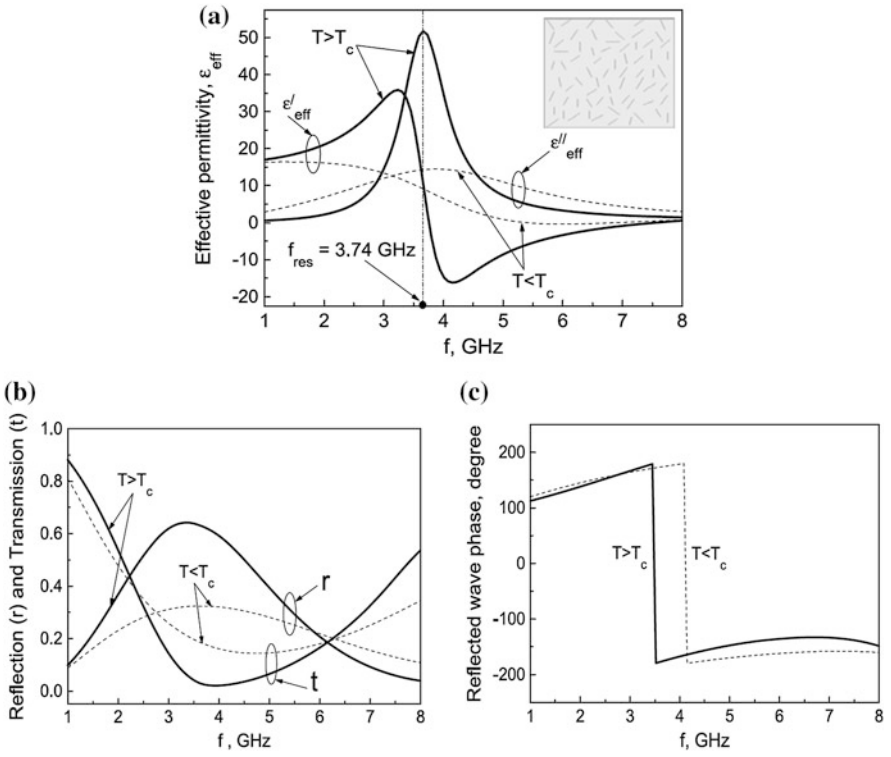


**Fig. 11.47** **a** Calculated dispersion spectra of resonance complex effective permittivity in the vicinity of antenna resonance under the influence of temperature: the *inset* shows the schematic configuration of the composite. **b** Typical transmission and reflection spectra under the influence of temperature. **c** Typical reflection phase spectra under the influence of temperature. [18]

of the stress or magnetic field, there is an anomalous dispersion of $\varepsilon'(f)$ and relaxation/resonance transformation when $T$ exceeds $T_c$. All these features demonstrate strong temperature effects, which can be exploited for temperature sensing. A very promising application is to embed these microwires into the pre-form of polymer laminates. The microwires can then serve as self-regulating heating elements in the microwave curing process, which is believed to be much more efficient than conventional curing methods [128]. Meanwhile, with proper choice of composition and tailoring, the wires can be made highly sensitive [129] to the temperature to be applied for process monitoring, which remains a challenging issue in composite manufacture [130]. In addition, the wires remain as stress-sensing elements in the cured composites for various kinds of structural application. With increasing use of advanced fibre-reinforced composites in industry [131], the addition of microwires may well renovate the composite industry to some extent.

Through most of this text, we have emphasised the basic physical principles underlying the tunable behaviour of the microwire composites. By examining individual cases of a generic or specific nature, we hoped to suggest the practical importance and versatility of the microwire composites for tunable devices at the microwave frequency range of considerable technical interest. We believe these examples are only the tip of an iceberg of possibilities that are yet to be discovered. In this sense, the chapter may also serve to stimulate the imaginations of researchers in diverse fields who will, in the end, turn the application potential afforded by this kind of microwave tunable composites into realities.

## References

1. Born M, Wolf E (1968) Principles of optics, 4th edn. Pergamon, New York
2. Makhnovskiy DP, Panina LV (2003) Field dependent permittivity of composite materials containing ferromagnetic wires. J Appl Phys 93:4120–4129
3. Lagarkov AN, Matytsin SM, Rozanov KN, Sarychev AK (1998) Dielectric properties of fiber-filled composites. J Appl Phys 84:3806–3814
4. Liu L, Matitsine SM, Gan YB, Rozanov KN (2005) Effective permittivity of planar composites with randomly or periodically distributed conducting fibers. J Appl Phys 98:063512–063517
5. Lagarkov AN, Sarychev AK (1996) Electromagnetic properties of composites containing elongated conducting inclusions. Phys Rev B 53:6318–6336
6. Pendry JB, Holden AJ, Stewart WJ, Youngs I (1996) Extremely low frequency plasmons in metallic mesostructures. Phys Rev Lett 76:4773–4776
7. Sarychev AK, Shalaev VM (2000) Electromagnetic field fluctuations and optical nonlinearities in metal-dielectric composites. Phys Rep 335:275–371
8. Makhnovskiy DP, Panina LV, Mapps DJ (2001) Field-dependent surface impedance tensor in amorphous wires with two types of magnetic anisotropy: helical and circumferential. Phys Rev B 63:144424
9. Makhnovskiy DP, Panina LV (2005) Field and stress tunable microwave composite materials based on ferromagnetic wires. In: MurrayNova VN (ed) Progress in ferromagnetism research. Science Publishers Inc, Hauppauge

10. Panina LV, Sandacci SI, Makhnovskiy DP (2005) Stress effect on magnetoimpedance in amorphous wires at gigahertz frequencies and application to stress-tunable microwave composite materials. J Appl Phys 97:013701–013706
11. Makhnovskiy DP, Panina LV, Garcia C, Zhukov AP, Gonzalez J (2006) Experimental demonstration of tunable scattering spectra at microwave frequencies in composite media containing Cofepris glass-coated amorphous ferromagnetic wires and comparison with theory. Phys Rev B 74:064205
12. Torcunov AV, Baranov SA, Larin VS (1999) The internal stresses dependence of the magnetic properties of cast amorphous microwires covered with glass insulation. J Magn Magn Mater 196–197:835–836
13. Adenot AL, Deprot S, Bertin F, Bois D, Acher O (2004) Magneto-elastic anisotropy of ferromagnetic glass-coated microwires. J Magn Magn Mater 272–276:E1115–E1116
14. Panina L, Mohri K, Uchiyama T, Noda N, Bushida K (1995) Giant magneto-impedance in Co-rich amorphous wires and films. IEEE Trans Magn 31:1249–1260
15. Sandacci S, Makhnovskiy D, Panina L, Larin V (2005) Stress-dependent magnetoimpedance in Co-based amorphous wires with induced axial anisotropy for tunable microwave composites. IEEE Trans Magn 41:3553–3555
16. Sarychev A, Shalaev V (2007) Electrodynamics of metamaterials. World Scientific Publishing Co. Pte. Ltd., Singapore
17. Shalaev VM, Cai W, Chettiar UK, Yuan HK, Sarychev AK, Drachev VP, Kildishev AV (2005) Negativeindex of refraction in optical metamaterials. Opt Lett 30:3356–3358
18. Makhnovskiy D, Panina L (2007) Free-space microwave testing of stress and temperature distributions in composite materials incorporating ferromagnetic wires. In: The XII electromagnetic nondestructive evaluation conference (ENDE-2007), Cardiff, UK
19. Makhnovskiy D, Panina L (2005) Tuneable microwave composites based on ferromagnetic wires. http://www.microwirescom/Surveyphp November 2005
20. Qin F, Peng H (2010) Macro-composites containing ferromagnetic microwires for structural health monitoring. Nano Commun Netw 1:126–130
21. Qin F, Peng HX, Tang J, Qin LC (2010) Ferromagnetic microwires enabled polymer composites forsensing applications. Compos A Appl Sci Manuf 41:1823–1828
22. Qin FX, Pankratov N, Peng HX, Phan MH, Panina LV, Ipatov M, Zhukova V, Zhukov A, Gonzalez J (2010) Novel magnetic microwires-embedded composites for structural health monitoring applications. J Appl Phys 107:09A314–09A314-3
23. Qin FX, Brosseau C, Peng HX, Wang H, Sun J (2012) In situ microwave characterization of microwire composites with external magnetic field. Appl Phys Lett 100:192903
24. Starostenko S, Rozanov K, Osipov A (2006) Microwave properties of composites with glass coated amorphous magnetic microwires. J Magn Magn Mater 298:56–64
25. Starostenko SN, Rozanov KN (2009) Microwave screen with magnetically controlled attenuation. Prog In Electromagnet Res 99:405–426
26. Starostenko SN, Rozanov KN, Osipov AV (2004) Microwave spectra of composites with an ordered amorphous microwire. J Commun Technol Electron 49:1399–1404
27. Qin FX, Peng HX, Popov VV, Panina LV, Ipatov M, Zhukova V, Zhukov A, Gonzalez J (2011) Stress tunable properties of ferromagnetic microwires and their multifunctional composites. J Appl Phys 108:07A310
28. Shin KH, Inoue M, Arai KI (1999) Strain sensitivity of highly magnetostrictive amorphous films for use in microstrain sensors. J Appl Phys 85:5465–5467
29. Tagantsev AK, Sherman VO, Astafiev KF, Venkatesh J, Setter N (2003) Ferroelectric materials for microwave tunable applications. J Electroceram 11:5–66
30. Giere A, Zheng Y, Maune H, Sazegar M, Paul F, Zhou X, Binder JR, Muller S, Jakoby R (2008) Tunable dielectrics for microwave applications. In: 2008 17th IEEE international symposium on the applications of ferroelectrics, vol 2, pp 1–2
31. Laur V, Rousseau A (2006) At microwave frequencies for tunable applications. Circ Des 53:2280–2286

32. Qin F, Peng HX, Prunier C, Brosseau C (2010) Mechanical–electromagnetic coupling of microwire polymer composites at microwave frequencies. Appl Phys Lett 97:153502–153503
33. Ghodgaonkar D, Varadan V, Varadan V (1989) A free-space method for measurement of dielectric constants and loss tangents at microwave frequencies. IEEE Trans Instrum Meas 38:789–793
34. Bryant G (1993) Principles of microwave measurements. IEE Electrical Measurement Series 5. ISBN 0-86341-296-3
35. Varadan VV, Jose KA, Varadan VK (2000) In sutimicrowave characterization of nonplanar dielectric objects. IEEE T Microw Theor 48:388–394
36. Hollinger RD, Jose KA, Tellakula A, Varadan VV, Varadan VK (2000) Microwave characterization of dielectric materials from 8 to 110 GHz using a free-space setup. Microwave Opt Technol Lett 26:100–105
37. Trabelsi S, Nelson S (2003) Free-space measurement of dielectric properties of cereal grain and oilseed at microwave frequencies. Meas Sci Technol 14:589–600
38. ELIRI Institute, Chisinau, Republic of Moldova. http://eliri.md/eng/about.htm
39. Search "application note 1304-07" at http://www.home.agilent.com
40. Agilent85071E Materials Measurement Software at www.agilent.com/find/mate-rials
41. Makhnovskiy D, Zhukov A, Zhukova V, Gonzalez J (2008) Tunable and self-sensing microwave composite materials incorporating ferromagnetic microwires. Adv Sci Tech 54:201–210
42. Christian B, Philippe T (2005) Instrumentation for microwave frequency-domain spectroscopy of filled polymers under uniaxial tension. Meas Sci Technol 16:1823
43. Salahun E, Queffelec P, Le Floch M, Gelin P (2001) A broadband permeameter for "in situ" measurements of rectangular samples. IEEE Trans Magn 37:2743–2745
44. Phan MH, Peng HX (2008) Giant magnetoimpedance materials: fundamentals and applications. Prog Mater Sci 53:323–420
45. Yelon A, Melo LGC, Ciureanu P, Ménard D (2002) High-frequency behavior of magnetically soft wires. J Magn Magn Mater 249:257–263
46. Yelon A, Menard D, Britel M, Ciureanu P (1996) Calculations of giant magnetoimpedance and of ferromagnetic resonance response are rigorously equivalent. Appl Phys Lett 69:3084–3085
47. Acher O, Jacquart PM, Boscher C (1994) Investigation of high frequency permeability of thin amorphous wires. IEEE Trans Magn 30:4542–4544
48. Britel MR, Menard D, Melo LG, Ciureanu P, Yelon A, Cochrane RW, Rouabhi M, Cornut B (2000) Magnetoimpedance measurements of ferromagnetic resonance and antiresonance. Appl Phys Lett 77:2737–2739
49. Sandacci S, Makhnovskiy D, Panina L (2004) Valve-like behavior of the magnetoimpedance in the GHz range. J Magn Magn Mater 272–276:1855–1857
50. Vazquez M, Adenot-Engelvin AL (2009) Glass-coated amorphous ferromagnetic microwires at microwave frequencies. J Magn Magn Mater 321:2066–2073
51. de Cos D, Lepalovskij V, Kurlyandskaya G, García-Arribas A, Barandiarán J (2008) High-frequencymagnetoimpedance in multilayer thin films with longitudinal and transverse anisotropy. J Magn Magn Mater 320:e954–e957
52. Labrador A, Gómez-Polo C, Pérez-Landazábal JI, Zablotskii V, Ederra I, Gonzalo R, Badini-Confalonieri G, Vázquez M (2010) Magnetotunable left-handed FeSiB ferromagnetic microwires. Opt Lett 35:2161–2163
53. Vázquez M (2001) Giant magneto-impedance in soft magnetic "Wires". J Magn Magn Mater 226–230:693–699
54. Garcia-Miquel H, Carbonell J, Boria V, Sánchez-Dehesa J (2009) Experimental evidence of lefthanded transmission through arrays of ferromagnetic microwires. Appl Phys Lett 94:054103
55. Garcia-Miquel H, Carbonell J, Sanchez-Dehesa J (2010) Left handed material based on amorphous ferromagnetic microwires tunable by dc current. Appl Phys Lett 97:094102

56. Brosseau C (2003) Computational electromagnetics and the rational design of new dielectric heterostructures. Prog Mater Sci 48:373–456
57. Tinga W (1992) Mixture laws and microwave-material interactions. Elsevier, Amsterdam, pp 1–36
58. Brosseau C (2008) Prospects in filled polymers engineering: mesostructure, elasticity network, and macroscopic properties. Research Signpost, Trivandrum
59. Qin FX, Peng HX, Phan MH, Panina LV, Ipatov M, Zhukov A (2012) Effects of wire properties on the field-tunable behaviour of continuous-microwire composites. Sens Actuators, A 178:118–125
60. Panina LV, Ipatov M, Zhukova V, Zhukov A, Gonzalez J (2011) Magnetic field effects in artificial dielectrics with arrays of magnetic wires at microwaves. J Appl Phys 109:053901
61. Zhukova V, Ipatov M, Zhukov A, Gonzalez J, Blanco J (2007) GMI effect in ultra-thin glass-coated Co-rich amorphous wires. Sens Actuators, B 126:232–234
62. Zhukov A, Zhukova V, Blanco JM, Cobeno AF, Vazquez M, Gonzalez J (2003) Magnetostriction in glass-coated magnetic microwires. J Magn Magn Mater 258–259: 151–157
63. Larin VS, Torcunov AV, Zhukov A, Gonzalez J, Vazquez M, Panina L (2002) Preparation and properties of glass-coated microwires. J Magn Magn Mater 249:39–45
64. Chiriac H (2001) Preparation and characterization of glass covered magnetic wires. Mater Sci Eng, A 304–306:166–171
65. Qin F, Peng H, Phan M (2010) Influence of varying metal-to-glass ratio on GMI effect in amorphous glass-coated microwires. Solid State Commun 150:114–117
66. Zhukova V, Ipatov M, Zhukov A (2009) Thin magnetically soft wires for magnetic microsensors. Sensors 9:9216–9240
67. Zhukov A, Zhukova V (2009) Magnetic properties and applications of ferromagnetic mircowires with amorphous and nanocrystalline structure. Nova Science Publishers, Inc., New York. (Qin, Phan and Peng, submitted to Springer)
68. Vazquez M (2007) Handbook of magnetism and advanced magnetic materials, vol 4. Novel Materials. Wiley. Advanced Magnetic Microwires, 1–29
69. Qin FX, Peng HX (2013) Ferromagnetic microwires enabled multifunctional composite materials. Prog Mater Sci 58:183–259
70. Panina L, Ipatov M, Zhukova V, Zhukov A, Gonzalez J (2010) Microwave metamaterials with ferromagnetic microwires. Appl Phys A Mater Sci Process 103:653–657
71. Ipatov M, Zhukova V, Panina LV, Zhukov A (2009) Ferromagnetic microwires composite metamaterials with tuneable microwave electromagnetic parameters. PIERS Proc 5:586–590
72. Peng H, Qin F, Phan MH, Tang J, Panina L, Ipatov M, Zhukov A, Zhukova V, Gonzalez J (2009) Co-based magnetic microwire and field-tunable multifunctional macro-composites. J Non-Cryst Solids 355:1380–1386
73. Acher O, Ledieu M, Adenot AL, Reynet O (2003) Microwave properties of diluted composites made of magnetic wires with giant magneto-impedance effect. IEEE Trans Magn 39:3085–3090
74. Zou TC, Zhao NQ, Shi C (2007) Design of activated carbon fibres/epoxy resin composites. J Funct Mater Dev 13:54–58
75. Qin FX, Peng HX, Fuller J, Brosseau C (2012) Magnetic field-dependent effective microwave properties of microwire-epoxy composites. Appl Phys Lett 101:152905
76. Qin FX, Peng HX, Phan MH, Panina LV, Ipatov M, Zhukova V, Zhukov A, Gonzalez J (2011) Smartcomposites with short ferromagnetic microwires for microwave applications. IEEE Trans Magn 47:4481–4484
77. Liu L, Kong L, Lin G, Matitsine S, Deng C (2008) Microwave permeability of ferromagnetic microwires composites/metamaterials and potential applications. IEEE Trans Magn 44: 3119–3122
78. Zhang Z, Wang C, Zhang Y, Xie J (2010) Microwave absorbing properties of composites filled with glass-coated $Fe_{69}Co_{10}Si_8B_{13}$ amorphous microwire. Mater Sci Eng B 175: 233–237

79. Qin FX, Quere Y, Brosseau C, Wang H, Liu JS, Sun JF, Peng HX (2013) Two-peak feature of the permittivity spectra of ferromagnetic microwire/rubber composites. Appl Phys Lett 102:122903
80. Baranov S (2009) Radioabsorption properties of amorphous microwires. Moldavian J Phys Sci 8:332–336
81. Liberal I, Nefedov I, Ederra I, Gonzalo R, Tretyakov S (2011) Electromagnetic response and homogenization of grids of ferromagnetic microwires. J Appl Phys 110:064909
82. Wang H, Xing D, Wang X, Sun J (2011) Fabrication and characterization of melt-extracted co-based amorphous wires. Metall Mater Trans A 42:1103–1108
83. Nagase T, Umakoshi Y (2010) Formation of melt-extracted wire of fëccücsicb alloy with corewire/surface-cover-layer structure by arc-melt-type melt-extraction method. J Alloys Compd 495:L1–L4
84. Wang H, Qin FX, Xing D, Cao F, Wang XD, Peng H, Sun J (2012) Relating residual stress and microstructure to mechanical and GMI properties in cold-drawn co-based amorphous microwires. Acta Mater 60:5425–5436
85. Garcia C, Zhukova V, Zhukov A, Usov N, Ipatov M, Gonzalez J, Blanco J (2007) Effect of interaction on giant magnetoimpedance effect in a system of few thin wires. Sens Lett 5(3):10–12
86. Arunachalam K, Melapudi V, Udpa L, Udpa S (2006) Microwave NDT of cement-based material susing far-field reflection coefficients. NDT & E Int 39:585–593
87. Reynolds W (1985) Nondestructive testing (NDT) of fibre-reinforced composite materials. Mater Des 5:256–270
88. Scott I, Scala C (1982) A review of non-destructive testing of composite materials. NDT Int 15:75–86
89. Prakash R (1980) Non-destructive testing of composites. Composites 11:217–224
90. Henneke E (1990) Ultrasonic nondestructive evaluation of advanced composites. Nondestr Test Fiber-Reinf Plast Compos 2:55–159
91. Adams R, Cawley P (1988) A review of defect types and nondestructive testing techniques for composites and bonded joints. NDT Int 21:208–222
92. Burke S, McKcousland S, Scala C (1994) Nondestructive characterization of advanced composite materials. Mater Forum 18:85–109
93. Prassianakis I, Prassianakis N (2004) Ultrasonic testing of non-metallic materials: concrete and marble. Theoret Appl Fract Mech 42:191–198
94. Garnier C, Pastor ML, Eyma F, Lorrain B (2011) The detection of aeronautical defects in situ on composite structures using non destructive testing. Compos Struct 93:1328–1336
95. Maser K, Roddis W (1980) Principles of thermography and radar for bridge deck assessment. J Transp Eng ASCE 116:583–600
96. Pastor M, Balandraud X, Grédiac M, Robert J (2008) Applying infrared thermography to study the heating of 2024-t3 aluminium specimens under fatigue loading. Inf Phys Technol 51:505–515
97. Liao TW, Li Y (1998) An automated radiographic NDT system for weld inspection: part II–flaw detection. NDT and E Int 31:183–192
98. Graeme W, Jr, Eizember A, Douglass J (1990) Digital image analysis of nondestructive test in gradiographs. Mater Eval 117–120
99. Mast JE, Lee H, Murtha JP (1992) Application of microwave pulse-echo radar imaging to then on destructive evaluation of buildings. Int J Imaging Syst Technol 4:164–169
100. Pieraccini M, Luzi G, Mecatti D, Noferini L, Atzeni C (2003) A microwave radar technique for dynamic testing of large structures. IEEE Trans Microwave Theor Tech 51:1603–1609
101. Hughes D, Kazemi M, Marler K, Zoughi R, Myers J, Nanni A (2002) Microwave detection of delaminations between fiber reinforced polymer (FRP) composite and hardened cement paste. AIP Conf Proc 615:512–519
102. Bois K, Benally A, Zoughi R (2000) Microwave near-field reflection property analysis of concrete for material content determination. IEEE Trans Instrum Measur 49:49–55

103. Matsuzaki R, Melnykowycz M, Todoroki A (2009) Antenna/sensor multifunctional composites for the wireless detection of damage. Compos Sci Tech 69:2507–2513
104. Aragoneses P, Blanco JM, Cobeno AF, Dominguez L, Gonzalez J, Zhukov A, Larin V (1999) Stress dependence of the switching field in co-rich amorphous microwires. J Magn Magn Mater 196–197:248–250
105. Bayri N, Atalay S (2004) Giant stress-impedance effect in $Fe_{71}Cr_7Si_9B_{13}$ amorphous wires. J Alloy Compd 381:245–249
106. Cobeno AF, Zhukov A, Blanco JM, Larin V, Gonzalez J (2001) Magnetoelastic sensor based on GMI of amorphous microwire. Sens Actuators, A 91:95–98
107. Garcia C, Chizhik A, Zhukov A, Zhukova V, Gonzalez J, Blanco J, Panina L (2007) Influence of torsion and tensile stress on magnetoimpedance effect in fe-rich amorphous microwires at high frequencies. J Magn Magn Mater 316:e896–e899
108. Gonzalez J, Chen A, Blanco J, Zhukov A (2002) Effect of applied mechanical stresses on the impedance response in amorphous microwires with vanishing magnetostriction. Phys Status Solidi A 189:599–608
109. Knobel M, Vasquez M, Sanchez ML, Hernando A (1997) Effect of tensile stress on the field response of impedance in low magnetostriction amorphous wires. J Magn Magn Mater 169:89–97
110. Knobel M, Sanchez ML, Vazquez M (1995) Stress dependence of the giant magneto-impedance effect in amorphous wires. J Phys: Condens Matter 7:L115–L120
111. Antonov AS, Borisov VT, Borisov OV, Prokoshin AF, Usov NA (2000) Residual quenching stresses in glass-coated amorphous ferromagnetic microwires. J Phys D Appl Phys 33:1161
112. Aranda GR, Usov NA, Zhukova V, Zhukov A, Gonzalez J (2008) Magnetostatic properties of co-rich amorphous microwires: theory and experiment. Phys Status Solidi A 205:1800–1804
113. Zuberek R, Szymczak H, Gutowski M, Zhukov A, Zhukova V, Usov NA, Garcia K, Vazquez M (2007) Internal stress influence on FMR in amorphous glass-coated microwires. J Magn Magn Mater 316:e890–e892
114. Zhukov A, Cobeno AF, Gonzalez J, Torcunov A, Pina E, Prieto MJ, Blanco JM, Larin V, Baranov S (1999) Ferromagnetic resonance, magnetic behaviour and structure of fe-based glasscoated microwires. J Magn Magn Mater 203:238–240
115. Valenzuela R, Zamorano R, Alvarez G, Gutierrez M, Montiel H (2007) Magnetoimpedance, ferromagnetic resonance, and low field microwave absorption in amorphous ferromagnets. J Non-Cryst Solids 353:768–772
116. Montiel H, Alvarez G, Gutierrez M, Zamorano R, Valenzuela R (2006) The effect of metal-to-glass ratio on the low-field microwave absorption at 9.4 GHz of glass-coated CoFeBSi microwires. IEEE Trans Magn 42:3380–3382
117. Chiriac H, Colesniuc CN, Ovari TA, Ticussan M (1999) In situ investigation of the magnetization processes in amorphous glass-covered wires by ferromagnetic resonance measurements. J Appl Phys 85:5453–5455
118. Melik R, Unal E, Perkgoz NK, Puttlitz C, Demir HV (2009) Metamaterial-based wireless strain sensors. Appl Phys Lett 95:011106
119. Sakai K, Asano N, Wada Y, Yoshikado S (2010) Composite electromagnetic wave absorber made of soft magnetic material and polystyrene resin and control of permeability and permittivity. J Eur Ceram Soc 30:347–353
120. Xu X, Qing A, Gan YB, Feng YP (2007) An experimental study on electromagnetic properties of random fiber composite materials. Microwave Opt Technol Lett 49:185–190
121. Qin F, Popov V, Peng HX (2011) Stress tunable microwave absorption of ferromagnetic microwires for sensing applications. J Alloy Compd 509:9508–9512
122. Qin F, Brosseau C, Peng HX (2011) In situ microwave characterization of microwire composites under mechanical stress. Appl Phys Lett 99:252902
123. Kim B, Lee J, Yu I (2003) Electrical properties of single-wall carbon nanotube and epoxy composites. J Appl Phys 94:6724–6728

124. Chiriac H, Marinescu CS, Ovari TA (1999) Temperature dependence of the magneto-impedance effect. J Magn Magn Mater 196–197:162–163
125. Kim Y, Cho W, Kim T, Kim C, Lee H (1998) Temperature dependence of magnetoimpedance effect in amorphous $Co_{66}Fe_4Nib_{14}Si_{15}$ ribbon. J Appl Phys 83:6575–6577
126. Chen G, Yang XL, Zeng L, Yang JX, Gong FF, Yang DP, Wang ZC (2000) High-temperature giant magnetoimpedance in fe-based nanocrystalline alloy. J Appl Phys 87:5263–5265
127. Zhukova V, Ipatov M, Zhukov A, Varga R, Torcunov A, Gonzalez J, Blanco J (2006) Studies of magnetic properties of thin microwires with low curie temperature. J Magn Magn Mater 300:16–23
128. Papargyris D, Day R, Nesbitt A, Bakavos D (2008) Comparison of the mechanical and physical properties of a carbon fibre epoxy composite manufactured by resin transfer moulding using conventional and microwave heating. Compos Sci Technol 68:1854–1861
129. Zhukova V, Blanco JM, Ipatov M, Zhukov A, Garcia C, Gonzalez J, Varga R, Torcunov A (2007) Development of thin microwires with low curie temperature for temperature sensors applications. Sens Actuators, B 126:318–323
130. Fernando G, Degamber B (2006) Process monitoring of fibre reinforced composites using optical fibre sensors. Int Mater Rev 51(42):65–106
131. Serkov A, Radishevskii M (2008) Status and prospects for production of carbon fibres based on polyacrylonitrile. Fibre Chem 40:24–31